Lithos 380–381 (2021) 105849

Contents lists available at ScienceDirect

Lithos

journal homepage: www.elsevier.com/locate/lithos

Research Article

Disequilibrium phenocrystic assemblage within dacites reveals magma mixing and stratified chamber after crustal assimilation at El Hoyazo volcano, SE Spain

Hiyori Hiwatashi [a], Masao Ban [a,*], Antonio M. Álvarez-Valero [b], Leo M. Kriegsman [c,d], Motohiro Sato [a]

[a] Department of Science, Yamagata University, Japan
[b] Department of Geology, University of Salamanca, Spain
[c] Department of Research and Education, Naturalis Biodiversity Center, Leiden, the Netherlands
[d] Department of Earth Sciences, Faculty of Geosciences, Utrecht University, the Netherlands

ARTICLE INFO

Article history:
Received 15 May 2020
Received in revised form 13 October 2020
Accepted 16 October 2020
Available online 20 October 2020

Keywords:
Magma injections
Hornblende
Crustal assimilation
Magmatic inclusions/enclaves
Rapid magma ascent
Resorption textures

ABSTRACT

In volcanic areas where evolved and primitive magmas coexist, it is common to observe evidence of magma mixing. At the Neogene silicic volcano of El Hoyazo in SE Spain, the detailed petrological and geochemical characteristics of the phenocrysts (plagioclase, biotite, amphibole and pyroxene) as well as their host dacitic lavas allow the reconstruction of the structure of the magma plumbing system. Microtextures, modal abundances, and geochemistry of zoned phenocrysts reveal a stratified magma composed of (i) high-SiO_2 dacites with An-poor (<50%) plagioclase and Mg-poor biotite; (ii) high-SiO_2 andesites with intermediate-An (50–70%) plagioclase and intermediate-Mg biotite; and (iii) an andesitic magma with An-rich (>80%) plagioclase, Mg-rich pyroxene, and tschermakitic hornblende, whose zoning records different crystallization depths during magma ascent. Evidence from the hornblende varieties and from mafic enclaves or inclusions indicates that the stratified chamber was repeatedly injected by hotter magmas from greater depth.

1. Introduction

Magma chambers are highly dynamic settings where multiple processes, each variable in time, interact. As a result, the chemical composition, including the volatile and mineral content of the magma, often show complex changes in time that have a major impact on the type of volcanism at the surface. One of the main processes is the injection of magma pulses from greater depth into a subvolcanic reservoir which can fractionate, become mingled or thoroughly mixed with earlier melt batches, and even propel the eruptive activity (e.g., Pallister et al., 1992; Sparks et al., 1977; Williamson et al., 2010). Magma mixing is not a prerequisite for eruption. The mere intrusion of new magma into a shallower reservoir and related exsolution of volatiles may be sufficient to trigger an eruption by simply increasing the internal pressure of the chamber (e.g., Blake, 1981; Folch and Martí, 1998).

Evidence of mixing between two magmas (compositionally similar or different), with or without evidence at a macroscopic scale, can be inferred microscopically from the mode, texture, and chemistry of zoned phenocrysts (e.g. Johnson et al., 2008; Nishi et al., 2019). Chemical gradients can also help to constrain timescales of different processes because of potential diffusion kinetics (Albert et al., 2015, 2016).

Eruptions of mixed andesitic to dacitic volcanoes are normally related to complex petrological and geochemical histories that show a wide mixture of minerals and melts (e.g., Humphreys et al., 2006; Nakamura, 1995; Nishi et al., 2019; Reubi and Blundy, 2009; Zeck, 1970) and involve processes such as magma mixing, fractional crystallization and crustal assimilation. In order to advance in these aspects, we studied the phenocrysts (plagioclase, biotite, amphibole, and pyroxene) within dacites and andesites of the extinct Neogene volcano of El Hoyazo (SE Spain), combining petrological (petrography, mineral modes, mineral chemistry, and thermodynamics) and geochemical (whole rock and isotopic compositions) methods. Our results demonstrate that (i) these petrological-geochemical indicators reveal the structure of the magma plumbing system and its evolution until eruption; and (ii) a shallow crustal assimilated chamber was subjected to multiple injections of mafic magmas from deeper levels.

1.1. Geological setting: Previous petrological and geochemical information about the NVP and El Hoyazo volcano

El Hoyazo is a fossil submarine lava dome located in the Neogene Volcanic Province (NVP) of SE Spain, within the Internal Zones of the

* Corresponding author.
E-mail address: ban@sci.kj.yamagata-u.ac.jp (M. Ban).

https://doi.org/10.1016/j.lithos.2020.105849

Betic Cordillera in the western Mediterranean (Fig. 1). The adjacent Alborán Sea formed by lithospheric extension that started ca. 25 *Ma* during the Miocene evolution of the Betic Cordillera, within the framework of the convergence between the African and Eurasian plates (e.g., Benito et al., 1999; García-Dueñas et al., 1992; Turner et al., 1999; Vergés and Fernàndez, 2012; Vissers et al., 1995; Vissers and Meijer, 2012). The Miocene-Neogene volcanic zone of Cabo de Gata is mainly composed of interbedded volcanic and sedimentary materials (e.g., Fernández-Soler, 2001; Martín et al., 1996). The former are calc-alkaline rocks from submarine and subaerial volcanic eruptions, showing a wide compositional range of basaltic andesites, andesites, dacites, rhyodacites and rhyolites (Di Battistini et al., 1987; Fernández-Soler, 2001; Toscani et al., 1990). The most abundant volcanic rocks in the NVP are high-K calc-alkaline rocks, mostly andesites and dacites (Benito et al., 1999; Duggen et al., 2004; Fernández-Soler, 1996). The age of the NVP ranges from 17 to 5 *Ma* (Cesare et al., 2003; Duggen et al., 2004; Turner et al., 1999; Zeck et al., 1998).

El Hoyazo's atoll geomorphology displays a circular shape of ~0.7 km^2 and a ~ 500 m crater radius, overlain by reef carbonates. Dacites of El Hoyazo are porphyritic with >50 vol% of rhyolitic glassy matrix (both fresh and devitrified), phenocrysts of plagioclase, biotite, and minor orthopyroxene, amphibole, magnetite and quartz, and local xenocrysts of garnet, cordierite, and ilmenite. Cristobalite xenocrysts are also locally present in El Hoyazo (e.g., Molina et al., 2015). Previous studies of the dacites have described to some extent their mineralogy and chemistry (e.g., Fernández-Soler, 1996; Zeck, 1970), as well as their isotopic (Álvarez-Valero et al., 2016; Benito et al., 1999) and textural (Álvarez-Valero et al., 2016) features. These intermediate lavas contain up to 15 vol% crustal material (Zeck, 1970) in the form of granulite-facies xenoliths with a restitic bulk composition, being depleted in silica and enriched in aluminium and iron. The restite is the most studied material in this volcano (e.g., Álvarez-Valero et al., 2005, 2007, 2016; Álvarez-Valero and Kriegsman, 2007; Álvarez-Valero and Waters, 2010; Benito et al., 1999; Cesare et al., 1997; Duggen et al., 2004; Zeck, 1970). These metapelitic xenoliths were quenched immediately after eruption (e.g., Álvarez-Valero and Waters, 2010; Cesare et al., 1997; Zeck, 1970), and provide direct evidence of the partial crustal melting processes at depth (e.g., Álvarez-Valero and Kriegsman, 2007; Álvarez-Valero and Waters, 2010; Cesare et al., 1997; Zeck, 1970), leading to 35–60 wt% melt extraction (Cesare et al., 1997). Previous studies have concluded that the silicic lavas of El Hoyazo resulted from mixing at 13–19 km depth between the rhyolitic melt extracted from the partially melted crust and magmas derived from mafic underplating of the Betic Cordillera (e.g., Álvarez-Valero and Kriegsman, 2007; Benito et al., 1999; Duggen et al., 2004). Indeed, the melt composition in crystal inclusions and interstitial pockets within the xenoliths differs from the glass of the dacitic lavas by having lower Al/Si and higher K/Na ratios (Cesare et al., 1997). Magma mixing at 13–19 km depth beneath El Hoyazo occurred in two main episodes according to microstructures and age relationships in the xenoliths: (i) a first stage of migmatization and melt extraction where the rhyolite mixed with the primary mafic-intermediate magma to form the host dacites (Álvarez-Valero and Kriegsman, 2007; Duggen et al., 2004), which fits the observation of local quartz-diorite, basaltoid and quartz-gabbroic pockets embedded in the dacites (e.g., Benito et al., 1999); and (ii) a second, transiently heated wall-rock episode at the magma conduit that triggered the collapse of the crustal walls (Álvarez-Valero and Waters, 2010). This was followed by rapid (i.e., minutes to hours) magma ascent from depth to the surface during eruption (Álvarez-Valero et al., 2015; Álvarez-Valero and Waters, 2010; Pla and Álvarez-Valero, 2015). The new data in this paper build on these earlier studies and show that the magmatic evolution at El Hoyazo is even more complex, revealing a close link to the multiple andesite-dacite cycles observed in the volcanic suites of SE Spain (e.g., Soriano et al., 2016).

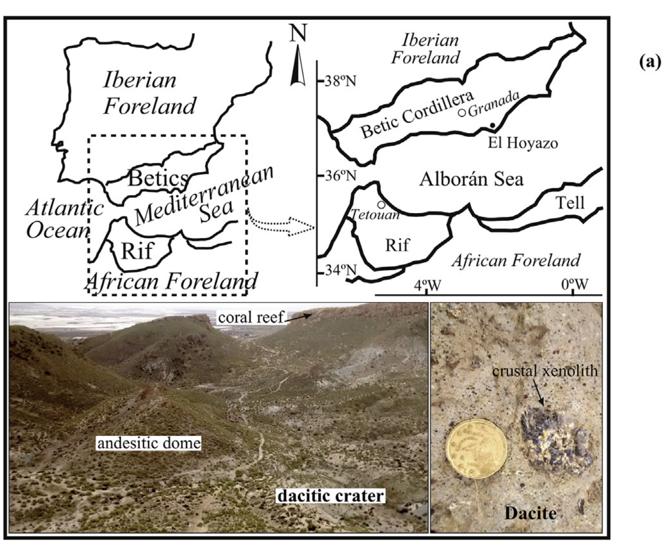

Fig. 1. Location of El Hoyazo volcano within the Betic Cordillera (SE Spain); and inner crater view from the northern rim.

2. Materials and methods

After petrographical analysis of dozens of lava samples, we selected eight representative dacites from El Hoyazo (Table 1) for further mineral chemistry and geochemical analysis. The samples were collected in the summer of 2016, and the location coordinates were not considered, as the dacites are randomly distributed within the entire outcrop without petrological or structural systematics. Samples HY1 and HY7a were divided into two sub-samples according to their notable banded structure in the groundmass, yet with the same mineral assemblages: darker (D) and lighter/whiter (W) parts (e.g., HY1; Fig. 2a–b).

Whole-rock major element and trace element concentrations were determined by X-ray fluorescence (XRF) analysis with a Rigaku RIX2000 spectrometer at Yamagata University. Operating conditions were 50 kV accelerating voltage and 50 mA current. The preparation method of the glass disks and the calibration method for major elements, as well as the calibration method for the trace elements, follow Yamada et al. (1995). The standards used in the analyses are the GSJ (Geological Survey of Japan) igneous rocks series. Analytical uncertainties are 5% for Nb, Zr, Y, Sr, Rb and Ni, 10% for V and Cr, and 5–15% for Ba. The range of uncertainties for a single element is based on the concentration range observed in standards.

Electron microprobe chemical analyses (EMPA) of minerals and glasses were performed with a JEOL JXA8900 wavelength-dispersive type electron probe microanalyser at Yamagata University, using natural and synthetic minerals as standards. Operating conditions were 15 kV accelerating voltage, a beam current of 10 nA (plagioclase) or

Table 1
Phenocryst and xenocryst assemblages within El Hoyazo lava samples.

Dacite sample	Phenocryst	Xenocryst	Inclusion or enclave
HY1	plg, bt, qtz, hbl		clot type
HY2	plg, bt, qtz	spl	plutonic
HY6	plg, bt, qtz, hbl		
HY7a	plg, bt, qtz, hbl, cpx, opx	crd, qtz	
HY7b	plg, bt, qtz	crd	mafic
HY8	plg, bt, qtz	ilm	
HY9	plg, bt, qtz	grt	mafic
HY10	plg, bt, qtz, hbl, cpx	qtz	clot type

Pl: plagioclase, Bt: biotite, Opx: orthopyroxene, Cpx: clinopyroxene, Amp: amphibole, Crd: Cordierite, Qtz: quartz, Spl: spinel, Grt: garnet, Ilm: ilmenite.

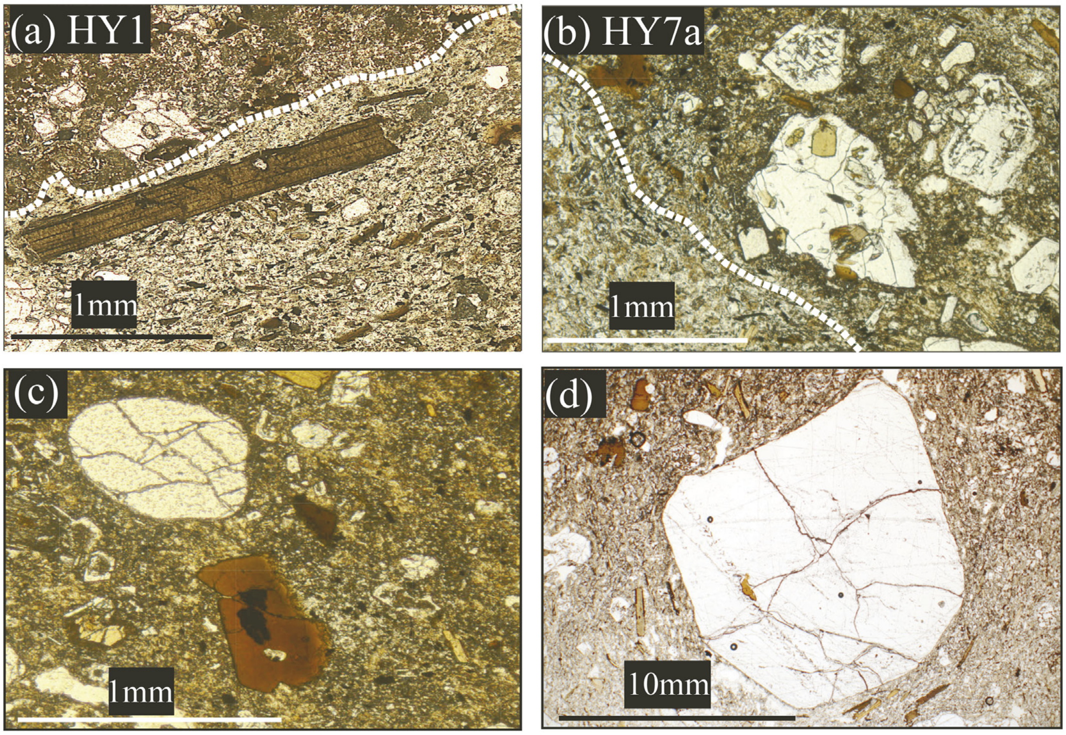

Fig. 2. Examples of banded structures (a) and (b) and quartz phenocryst (c) and xenocryst (d) (plane-polarized light microscopy views) in dacites from El Hoyazo volcano. Dashed line limits darker and whiter domains.

20 nA (all other minerals), and 10 s counting time for each element. All analyses were corrected using the oxide ZAF method.

For the stable isotopes analyses we used petrographical observations to select the samples with both the largest melt-inclusion-bearing crystals, and fresh glass with complete absence of secondary minerals, e.g., zeolites. For the glass samples we cut several centimeters of material from the surface to avoid any potential late isotopic modification by weathering. Finally, for the pheno- and xenocryst samples we crushed and sieved (>400 μm grain size) selected fragments, and manually separated the crystals and glass shards.

The hydrogen and oxygen isotopic analyses were carried out at the Servicio General de Análisis de Isótopos Estables (NUCLEUS - University of Salamanca, Spain). Oxygen in glass and phenocrysts was extracted by fluorination (Clayton and Mayeda, 1963) employing a Synrad 25 W CO_2 laser (Sharp, 1990) and ClF_3 as reagent (e.g., Borthwick and Harmon, 1982), and oxygen isotope ratios were measured on a VG-Isotech SIRA-II dual-inlet mass spectrometer. Both internal and international reference standards (NBS-28, NBS-30) were run to check accuracy and precision. Results are reported in $\delta^{18}O$ notation relative to Vienna Standard Mean Ocean Water (V-SMOW), using a $\delta^{18}O$ value of 9.6‰ for NBS-28 (quartz) for the mass spectrometer calibration. Long-term reproducibility for repeated determination of reference samples was better than ±0.2‰ (1σ).

D/H ratios were determined on another SIRA-II mass spectrometer on H_2 gas obtained by reduction over hot depleted-U of the water released by induction heating of samples. A vacuum line (Bigeleisen et al., 1952), following the procedures described by Godfrey (1962) with modifications (Jenkin, 1988), was used for gas extraction. Samples (i.e., glass and phenocrysts) were loaded into degassed platinum crucibles that were placed in quartz reaction tubes and heated under vacuum to 125 °C overnight to remove any adsorbed H_2O. Results are reported in δD notation relative to the V-SMOW standard, using a $\delta D = -66.7$‰ for NBS-30 (biotite) for the mass spectrometer calibration. The amount of H_2 recovery is known by a baratron gauge reading, which measures the total hydrogen (non-condensables) derived from water according to the ideal gas law. Then, we calculated the water content (% H_2O), as a function of the amount of H_2 obtained and the sample weight (wt%). Long-term reproducibility for repeated determination of reference samples was better than ±2‰ (1σ). Obtaining D/H values in phenocrysts (amphibole, plagioclase + quartz) requires a significant amount of gas released from melt/fluid inclusions. Due to the extreme difficulty to mechanicaly separate Qtz from Pl crystals, we performed analysis on Qtz-Pl mixtures, which represent the last melt that crystallized at the solidus.

For the pressure-temperature (P-T) estimates we utilized the XRF and EMPA data (Tables 2-6) to compute geothermobarometers (biotite, pyroxene and amphibole) of Henry et al. (2005), Putirka (2008), and Ridolfi and Renzulli (2012), respectively (Table 4).

3. Results

3.1. Petrography

All studied samples contain around 20% of phenocrysts within a hyalo-ophitic to hyalopilitic groundmass. The phenocryst assemblage

Table 2
Modal mineral abundance of phenocrysts and xenocrysts in the lava samples of El Hoyazo.

Dacite	Quartz	Plagioclase	Biotite	Pyroxene	Amphibole	Groundmass
HY1D	2.4	8.6	5.2	np	0.1	83.7
HY1W	2.5	6.4	7.1	np	0.3	83.7
HY7aD	6.3	2.5	7.4	tr	0.2	83.6
HY7aW	2.5	7.2	4.7	tr	0.1	85.5
HY7b	4.2	4.2	11.5	np	np	80.1
HY2	4.3	3.4	9.8	np	np	82.5
HY6	1.0	3.8	11.0	np	0.2	84.1
HY8	4.7	5.1	11.4	np	np	78.8
HY9	4.9	5.2	8.5	np	np	81.4
HY10	3.3	5.5	10.9	tr	0.1	80.2

tr: trace amount; np: not present.

Table 3
Representative chemical compositions (wt%) of plagioclase phenocrysts and groundmass.

Sample	Point	SiO_2	Al_2O_3	Fe_2O_3	MgO	CaO	Na_2O	K_2O	total	An	Type
HY1	1core	50.80	30.38	0.13	0.00	14.75	3.10	0.24	99.40	71	patchy
HY1	1rim	52.28	29.79	0.18	0.04	13.68	3.59	0.33	99.89	67	
HY1	2core	51.00	30.35	0.32	0.36	13.80	2.75	0.26	98.84	72	patchy
HY1	2rim	55.58	26.77	0.12	0.04	10.42	5.39	0.36	98.67	51	
HY1	3core light	53.16	28.92	0.09	0.06	12.80	4.30	0.28	99.62	61	oscillatory
HY1	3core dark	56.76	26.04	0.05	0.00	9.49	5.86	0.47	98.67	46	
HY1	3rim	52.26	29.67	0.14	0.01	13.53	3.92	0.30	99.83	64	
HY1	4core	57.39	25.66	0.08	0.01	8.87	6.10	0.46	98.57	43	homogeneous
HY1	4rim	58.34	25.54	0.05	0.01	8.42	5.94	0.55	98.85	42	
HY1	5core light	52.64	29.09	0.34	0.02	13.32	3.92	0.25	99.57	64	oscillatory
HY1	5core dark	57.39	25.50	0.41	0.33	8.54	5.44	0.60	98.21	45	
HY1	6core	47.36	32.16	0.12	0.03	17.77	1.43	0.09	98.95	87	patchy
HY1	6core2	48.22	31.80	0.07	0.00	16.59	1.96	0.11	98.75	82	
HY1	6rim	54.23	28.54	0.10	0.02	12.12	4.48	0.26	99.76	59	
HY1	8core	48.83	32.39	0.08	0.02	15.76	2.16	0.08	99.31	80	patchy
HY1	8rim	55.11	27.07	0.17	0.01	11.10	4.76	0.51	98.74	55	
HY1	9core	47.76	31.84	0.11	0.00	16.86	1.68	0.16	98.42	84	resorbed
HY1	9rim1	57.58	26.09	0.06	0.02	9.29	5.99	0.43	99.45	45	
HY1	10core	59.65	24.81	0.03	0.00	7.02	7.64	0.55	99.69	33	homogeneous
HY1	10rim	53.50	29.17	0.14	0.01	13.24	3.77	0.31	100.15	65	
HY2	1core	59.53	25.71	0.01	0.01	7.72	6.83	0.65	100.46	37	homogeneous
HY2	1rim	59.95	24.93	0.05	0.00	7.52	6.98	0.71	100.14	36	
HY2	2core light	53.34	30.03	0.07	0.00	12.36	4.10	0.28	100.18	61	oscillatory
HY2	2core dark	56.78	27.42	0.09	0.00	9.82	5.61	0.46	100.19	48	
HY2	3core light	54.50	29.08	0.08	0.01	11.56	4.95	0.32	100.49	55	oscillatory
HY2	3rim	55.10	29.06	0.15	0.01	11.77	4.93	0.35	101.36	56	
HY2	4core	55.03	27.94	0.08	0.01	10.45	5.47	0.39	99.35	50	homogeneous
HY2	4rim	56.51	28.18	0.09	0.00	10.46	5.36	0.42	101.02	51	
HY2	5core	48.27	32.90	0.10	0.01	16.62	2.15	0.08	100.12	81	resorbed
HY2	5rim	54.11	29.68	0.15	0.00	12.19	4.28	0.30	100.71	60	
HY2	6core	47.69	33.15	0.08	0.02	16.71	1.99	0.08	99.71	82	patchy
HY2	6rim	56.58	27.82	0.07	0.00	10.29	5.94	0.41	101.10	48	
HY2	7core	47.43	34.05	0.06	0.00	17.85	1.75	0.06	101.20	85	resorbed
HY2	7rim	56.09	28.54	0.08	0.00	10.39	5.13	0.38	100.60	52	
HY2	8core	48.98	32.42	0.10	0.03	15.88	2.50	0.16	100.07	77	resorbed
HY2	8rim	56.27	27.96	0.10	0.00	10.72	4.60	0.39	100.05	55	
HY2	9core dark	56.44	28.43	0.08	0.00	10.74	5.43	0.34	101.46	51	
HY7a	1core	60.29	25.04	0.05	0.00	7.46	7.03	0.60	100.46	36	homogeneous
HY7a	1rim	54.54	29.05	0.09	0.01	12.29	4.40	0.26	100.63	60	
HY7a	2core	46.18	34.62	0.27	0.01	18.24	1.13	0.04	100.49	90	resorbed
HY7a	2rim	56.93	27.92	0.18	0.02	10.64	5.82	0.45	101.96	49	
HY7a	3core light	57.28	26.88	0.05	0.01	10.06	5.95	0.39	100.63	47	oscillatory
HY7a	3core dark	58.98	26.33	0.04	0.01	9.18	6.66	0.49	101.68	42	
HY7a	3rim	57.32	27.33	0.09	0.02	9.72	5.73	0.42	100.62	47	
HY7a	4core1	60.87	24.73	0.07	0.00	7.12	7.30	0.53	100.61	34	homogeneous
HY7a	4core2	61.52	23.57	0.09	0.00	6.62	7.87	0.81	100.48	30	
HY7a	4rim	55.81	27.01	0.11	0.02	10.93	5.52	0.35	99.73	51	
HY7a	5core	49.11	32.30	0.21	0.02	16.63	1.95	0.18	100.39	82	resorbed
HY7a	5rim	53.81	28.11	0.12	0.01	12.26	4.31	0.35	98.98	60	
HY7a	6core	47.07	33.72	0.15	0.02	18.09	1.33	0.07	100.45	88	resorbed
HY7a	6rim	54.40	28.72	0.10	0.04	12.24	4.43	0.30	100.22	59	
HY7a	7core	48.13	32.96	0.06	0.00	17.18	1.93	0.07	100.33	83	resorbed
HY7a	7rim	57.39	27.31	0.10	0.01	10.41	6.29	0.39	101.90	47	
HY7a	8core	47.86	33.09	0.21	0.01	17.51	1.45	0.07	100.19	87	resorbed
HY7a	8rim	54.34	28.29	0.12	0.01	11.82	4.55	0.24	99.36	58	
HY7a	9core	51.65	30.41	0.05	0.02	13.62	3.59	0.16	99.50	67	patchy
HY7a	9rim1	58.21	25.84	0.04	0.02	8.50	6.72	0.51	99.82	40	
HY7a	10core	51.28	30.85	0.12	0.01	14.48	3.34	0.18	100.26	70	patchy
HY7a	10rim	57.87	26.86	0.13	0.04	9.83	5.68	0.45	100.85	48	
HY7b	1core	58.37	25.59	0.04	0.02	9.05	6.00	0.44	99.51	44	homogeneous
HY7b	1rim	61.71	23.34	0.05	0.04	5.85	8.07	0.53	99.59	28	
HY7b	2core	57.77	25.76	0.06	0.00	8.68	6.26	0.47	99.00	42	homogeneous
HY7b	2rim	57.98	24.82	0.05	0.04	8.49	6.34	0.76	98.48	41	
HY7b	3core	51.86	29.00	0.35	0.16	14.93	2.50	0.81	99.61	73	patchy
HY7b	3rim	55.10	29.14	0.09	0.02	12.13	4.81	0.34	101.63	57	
HY7b	4core	46.96	32.87	0.16	0.01	17.81	1.43	0.29	99.53	86	resorbed
HY7b	4rim	56.45	27.05	0.12	0.01	10.80	5.37	0.53	100.33	51	
HY7b	mafic. Inc. gm 1core	50.54	29.81	0.23	0.91	14.61	2.98	0.09	99.18	73	acicular
HY7b	mafic. Inc. gm 2core	49.06	30.44	0.21	0.05	14.62	2.83	0.35	100.28	73	acicular
HY8	1core dark1	53.32	29.30	0.08	0.00	11.85	4.29	0.310	99.15	59	oscillatory
HY8	1core dark2	53.71	29.95	0.06	0.02	12.59	4.32	0.262	100.91	61	
HY8	1rim	56.30	26.42	0.02	0.00	9.41	5.51	0.49	98.14	47	
HY8	2core light	49.99	32.00	0.08	0.03	14.76	2.84	0.152	99.85	74	oscillatory
HY8	2rim	56.04	27.27	0.08	0.00	9.69	5.64	0.457	99.18	47	

Table 3 (*continued*)

Sample	Point	SiO_2	Al_2O_3	Fe_2O_3	MgO	CaO	Na_2O	K_2O	total	An	Type
HY8	3core light	54.96	28.60	0.03	0.00	10.97	5.36	0.281	100.20	52	oscillatory
HY8	3core dark	61.76	24.21	0.01	0.02	5.56	7.90	0.639	100.10	27	
HY8	4core1	45.62	34.81	0.18	0.00	18.19	1.08	0.053	99.93	90	resorbed
HY8	4core2	47.03	33.91	0.18	0.04	16.80	1.91	0.119	99.99	82	
HY8	5patch	57.53	27.39	0.03	0.00	9.43	5.73	0.448	100.56	46	patchy
HY8	5rim	56.00	28.30	0.07	0.01	10.68	5.18	0.347	100.58	52	
HY8	6core light	59.33	25.90	0.01	0.00	7.68	6.56	0.613	100.09	38	oscillatory
HY8	6core dark	60.92	24.27	0.00	0.00	6.23	7.80	0.833	100.06	29	
HY8	7core	49.23	32.28	0.08	0.00	15.39	2.85	0.154	99.98	74	patchy
HY8	7rim	56.97	26.61	0.07	0.05	9.36	5.68	0.561	99.31	46	
HY8	8core1	45.09	34.01	0.14	0.02	17.57	1.35	0.062	98.24	87	resorbed
HY8	8core2	50.86	30.57	0.10	0.02	14.07	3.46	0.195	99.27	68	
HY8	9core1	47.68	34.24	0.14	0.00	17.17	1.82	0.087	101.13	84	patchy
HY8	9core2	51.75	29.92	0.08	0.00	12.92	3.89	0.283	98.85	64	
HY8	9rim	53.14	29.02	0.15	0.00	12.11	4.23	0.36	99.01	60	
HY8	10core1	46.57	34.49	0.13	0.07	17.83	1.20	0.130	100.42	88	resorbed
HY8	10core2	46.76	33.57	0.15	0.04	17.52	1.57	0.101	99.71	86	
HY9	1core light	51.70	30.22	0.04	0.01	13.40	3.94	0.178	99.48	65	oscillatory
HY9	1core dark	55.31	28.22	0.01	0.00	10.78	5.33	0.36	100.01	52	
HY9	1rim	53.13	30.25	0.07	0.03	12.82	4.38	0.228	100.91	61	
HY9	2core light	52.72	30.20	0.12	0.01	13.57	3.69	0.242	100.55	66	oscillatory
HY9	2core dark	57.82	27.69	0.04	0.00	9.32	5.90	0.434	101.20	45	
HY9	3core light	54.26	29.18	0.09	0.01	11.86	4.66	0.302	100.36	57	oscillatory
HY9	3core dark	55.76	28.24	0.02	0.00	11.09	5.07	0.327	100.51	54	
HY9	5core light	56.96	27.12	0.06	0.01	9.36	4.90	0.555	98.96	50	oscillatory
HY9	5core dark	57.54	26.92	0.06	0.01	8.47	6.00	0.44	99.45	43	
HY9	5rim	56.80	27.90	0.08	0.00	10.53	5.43	0.374	101.11	51	
HY9	6core1	53.16	29.11	0.35	0.07	13.98	2.49	0.952	100.11	71	patchy
HY9	6core2	47.77	32.24	0.14	0.01	16.08	2.27	0.14	98.66	79	
HY9	6rim	53.31	29.59	0.13	0.01	12.40	4.47	0.291	100.21	60	
HY9	7core light	56.05	27.16	0.13	0.08	9.63	5.43	0.455	98.92	48	oscillatory
HY9	7core dark	58.40	26.36	0.07	0.00	8.10	6.61	0.538	100.06	39	
HY9	8core	57.33	27.15	0.02	0.00	9.30	5.76	0.392	99.94	46	homogeneous
HY9	8rim	57.05	27.69	0.05	0.00	9.74	5.60	0.373	100.51	48	
HY9	8core light	51.52	30.79	0.05	0.01	13.72	3.57	0.170	99.83	67	oscillatory
HY9	8core dark	55.19	26.96	0.09	0.02	10.40	5.19	0.347	98.20	51	
HY9	10core	59.07	26.06	0.03	0.00	8.56	6.12	0.464	100.31	42	homogeneous
HY9	11core	52.39	29.90	0.04	0.01	13.13	3.99	0.216	99.68	64	patchy
HY9	11rim	54.29	28.42	0.05	0.00	11.68	4.63	0.324	99.39	57	
HY9	inclusion in biotite	56.00	27.55	0.18	0.00	10.38	5.21	0.47	99.79	51	
HY10	1core light	55.22	28.69	0.01	0.00	11.61	4.56	0.35	100.45	57	oscillatory
HY10	1rim	56.22	26.74	0.08	0.08	9.59	5.30	0.47	98.48	49	
HY10	2core dark	59.33	26.07	0.01	0.01	8.27	6.50	0.60	100.78	40	oscillatory
HY10	2core dark	58.39	25.87	0.07	0.02	8.11	6.42	0.68	99.56	39	
HY10	3core light	52.53	30.65	0.00	0.02	13.21	4.13	0.19	100.73	63	oscillatory
HY10	3core dark	57.53	27.48	0.07	0.02	9.68	5.99	0.36	101.13	46	
HY10	4core	51.85	31.25	0.06	0.00	14.03	3.72	0.19	101.09	67	patchy
HY10	4rim	56.47	27.48	0.06	0.00	9.69	5.46	0.37	99.53	48	
HY10	5core	46.74	33.68	0.03	0.01	17.37	1.57	0.09	99.49	85	patchy
HY10	5rim	55.85	28.45	0.00	0.00	10.15	5.36	0.32	100.13	50	
HY10	6core	51.29	31.81	0.07	0.00	14.31	3.23	0.16	100.87	70	patchy
HY10	6rim	56.48	28.70	0.06	0.00	10.89	5.10	0.29	101.52	53	
HY10	7core	47.45	33.58	0.10	0.00	16.86	1.77	0.12	99.87	83	patchy
HY10	7rim	56.92	27.22	0.00	0.00	9.12	6.03	0.40	99.69	44	
HY10	8core light	55.26	28.92	0.09	0.00	11.38	5.10	0.35	101.10	54	oscillatory
HY10	8core dark	57.30	28.03	0.07	0.01	9.71	5.76	0.41	101.29	47	
HY10	9core	46.42	34.75	0.11	0.02	17.92	1.37	0.07	100.65	87	resorbed
HY10	9rim	56.33	28.48	0.07	0.00	10.36	5.70	0.35	101.28	49	
HY10	10core	47.15	34.12	0.15	0.00	17.41	1.68	0.07	100.59	85	resorbed
HY10	10rim	55.29	28.46	0.06	0.01	11.25	4.90	0.36	100.33	55	
HY10	11patch	54.59	28.95	0.04	0.01	11.39	4.84	0.30	100.12	56	patchy
HY10	11rim	53.57	28.88	0.10	0.01	11.94	4.47	0.37	99.34	58	
HY10	12core	55.67	27.73	0.07	0.02	10.35	5.28	0.41	99.53	51	homogeneous
HY10	12rim	56.64	27.19	0.07	0.01	9.75	5.72	0.46	99.84	47	
HY10	13core light	55.60	29.79	0.00	0.01	10.81	4.67	0.30	101.18	55	oscillatory
HY10	13core dark	57.87	27.40	0.10	0.00	9.19	5.42	0.42	100.39	47	
HY10	inc. clot 1core1	47.05	33.33	0.31	0.01	17.36	1.56	0.10	99.71	86	resorbed
HY10	inc. clot 1core2	46.56	33.17	0.11	0.09	17.56	1.68	0.12	99.29	85	
HY10	inc. clot 1rim	52.51	30.18	0.05	0.01	13.81	3.65	0.23	100.44	67	
HY10	inc. clot 2core	46.05	34.53	0.07	0.04	17.67	1.44	0.09	99.89	87	resorbed
HY10	inc. clot 2rim	51.13	31.53	0.11	0.00	14.47	3.36	0.22	100.83	70	

An, anorthite%.

Table 4
Representative chemical compositions (wt%) of groundmass,and pyroxene, amphibole and biotite phenocrysts.

Sample	Point	SiO_2	TiO_2	Al_2O_3	FeO	MnO	MgO	CaO	Na_2O	K_2O	total	Mg#			
HY7a	core	55.74	0.08	1.49	16.59	0.34	27.23	0.40	0.02	0.03	101.92	75			
HY7a	rim1	55.53	0.09	1.52	16.71	0.33	26.87	0.41	0.02	0.02	101.49	74			
HY7a	rim2	54.07	0.11	1.54	16.13	0.33	26.45	0.45	0.00	0.02	99.09	75			
HY7b	inc. in bt	51.19	0.36	1.71	24.92	0.63	19.02	1.26	0.00	0.10	99.19	58			
HY1	inc. clot 1core	54.22	0.18	0.53	18.53	0.57	23.28	1.39	0.00	0.03	98.72	69			
HY1	inc. clot 1rim	53.56	0.12	1.05	26.03	0.66	19.73	0.63	0.01	0.06	101.85	57			
HY1	inc. clot 2core	54.06	0.24	0.77	19.09	0.41	24.41	1.47	0.00	0.01	100.47	70			
HY1	inc. clot 2rim	53.08	0.28	2.74	22.06	0.61	20.63	1.09	0.04	0.02	100.54	63			
HY1	inc. clot rim4	53.61	0.15	1.41	22.16	0.61	22.61	0.83	0.00	0.04	101.42	65			
HY1	inc. clot 5core	54.80	0.23	0.83	19.62	0.46	23.91	1.24	0.01	0.03	101.14	68			
HY1	inc. clot 5rim	53.44	0.22	1.56	22.45	0.55	19.93	1.26	0.00	0.03	99.44	61			
HY10	inc. clot 1core	51.48	0.55	5.65	17.15	0.31	24.16	0.99	0.04	0.01	100.32	72			
HY10	inc. clot 1middle	55.60	0.29	1.78	12.23	0.20	30.14	1.30	0.02	0.01	101.57	81			
HY10	inc. clot 1rim	52.44	0.13	1.35	28.72	0.77	17.24	0.60	0.00	0.06	101.30	52			
HY10	inc. clot 2core	55.59	0.14	1.06	13.00	0.24	29.51	1.43	0.00	0.01	100.97	80			
HY10	inc. clot 2rim	51.90	0.06	0.78	29.10	0.84	17.50	0.59	0.00	0.06	100.83	52			
HY10	inc. clot 3core	53.92	0.21	1.18	18.31	0.31	25.14	1.52	0.00	0.01	100.58	71			
HY10	inc. clot 3rim	51.52	0.08	0.88	30.37	0.88	16.80	0.65	0.01	0.05	101.22	50			
HY10	inc. clot 4core	55.78	0.26	1.29	13.35	0.10	28.79	1.24	0.01	0.02	100.82	79			
HY10	inc. clot 5core	51.73	0.09	1.89	28.27	0.80	18.07	0.49	0.00	0.01	101.36	53			
HY10	inc. clot 6core	51.29	0.32	2.12	25.18	0.48	19.15	1.02	0.00	0.02	99.57	58			
HY10	inc. clot 6rim	50.85	0.06	1.53	27.17	0.93	18.62	0.35	0.00	0.05	99.56	55			
HY7b	mafic inc.gm 1core	54.68	0.27	1.93	15.32	0.42	25.85	1.55	0.03	0.03	100.07	75			
HY7b	mafic inc.gm 2core	54.34	0.28	2.52	13.98	0.31	25.92	1.64	0.06	0.07	99.10	77			
HY9	mafic inc.gm 1core	54.18	0.24	1.40	15.90	0.24	26.08	1.43	0.00	0.00	99.48	75			
HY9	mafic inc.gm 2core	53.23	0.46	4.79	15.71	0.35	24.99	1.12	0.04	0.02	100.69	74			
Clinopyroxene															
Sample	Point	SiO_2	TiO_2	Al_2O_3	FeO	MnO	MgO	CaO	Na_2O	K_2O	total	Mg#			
HY7a	core	51.75	0.24	3.08	9.06	0.48	12.11	23.26	0.56	0.02	100.56	70			
HY7a	middle1	53.46	0.09	1.44	7.28	0.35	13.94	23.52	0.37	0.06	100.51	77			
HY7a	middle2	52.16	0.24	2.05	7.07	0.34	13.28	23.33	0.43	0.04	98.95	77			
HY7a	middle3	52.04	0.21	2.50	7.62	0.20	13.44	23.00	0.42	0.02	99.44	76			
HY7a	middle4	51.61	0.19	2.63	8.26	0.31	12.44	22.96	0.51	0.02	98.95	73			
HY7a	rim1	51.93	0.34	3.48	9.02	0.52	12.53	23.30	0.63	0.05	101.79	71			
HY7a	rim2	51.47	0.32	2.96	8.13	0.59	12.20	23.28	0.57	0.05	99.57	73			
HY10	lighter part1	51.81	0.47	2.50	6.39	0.20	15.06	23.18	0.26	0.03	99.90	81			
HY10	lighter part2	51.79	0.50	2.47	6.70	0.20	14.85	23.34	0.26	0.05	100.17	80			
HY10	darker part1	51.72	0.36	2.81	3.97	0.11	17.10	22.04	0.20	0.01	98.32	88			
HY10	darker part2	51.53	0.49	3.06	4.23	0.04	17.05	22.22	0.32	0.03	98.96	88			
Hornblende		wt%													
Sample	Point	SiO_2	TiO_2	Al_2O_3	Cr_2O_3	FeO	MnO	MgO	CaO	Na_2O	K_2O	total	Mg#	T(°C)	P(Kbar)
HY1	1core	45.83	1.36	9.75	0.02	13.18	0.31	13.05	11.21	1.22	1.08	96.99	64	855	2.25
HY1	1rim	46.69	1.70	9.07	0.00	9.83	0.19	14.66	11.28	1.36	0.76	95.54	73	851	2.02
HY1	2core	45.00	2.23	11.08	0.04	12.99	0.24	12.87	10.70	1.88	0.93	97.96	64	890	3.06
HY1	2rim	44.99	2.35	10.79	0.06	13.07	0.11	13.30	10.43	1.56	0.93	97.58	64	881	2.94
HY6	1core	45.28	1.88	11.71	0.00	13.23	0.20	12.82	10.41	1.36	1.06	97.93	63	888	3.63
HY6	1middle	44.92	1.42	12.11	0.03	13.86	0.24	11.66	10.77	1.20	0.87	97.08	57	885	3.59
HY6	1rim	44.63	1.59	12.10	0.02	15.28	0.19	11.59	10.52	1.43	0.91	98.27	63	854	2.83
HY6	2core	44.03	2.32	13.84	0.00	11.14	0.12	13.64	10.83	1.08	0.79	97.79	69	952	4.89
HY6	2middle1	44.04	2.22	13.65	0.00	11.65	0.19	13.10	10.60	1.97	0.85	98.26	67	941	4.82
HY6	2middle2	44.99	2.20	12.59	0.04	12.26	0.31	13.45	10.81	1.72	0.96	99.34	66	918	4.49
HY6	2middle3	45.74	2.02	12.06	0.00	14.15	0.25	11.98	10.68	1.49	0.85	99.22	60	882	3.56
HY6	2rim	46.67	1.47	11.08	0.00	13.78	0.17	12.52	10.47	1.34	0.78	98.27	62	856	2.91
HY6	3core	43.45	2.23	11.95	0.04	12.52	0.13	13.11	11.22	1.67	1.09	97.40	65	929	3.67
HY6	3rim	47.57	1.28	9.43	0.03	13.96	0.32	13.11	10.48	1.22	0.70	98.10	63	829	2.15
HY7a	1middle1	42.79	1.92	14.43	0.01	11.46	0.04	12.16	11.47	1.78	1.15	97.22	65	971	4.97
HY7a	1middle2	44.54	1.68	13.49	0.01	9.94	0.13	14.20	11.16	1.70	0.97	97.81	72	944	4.64
HY7a	2core	47.80	1.90	8.98	0.08	12.65	0.25	14.47	10.09	1.38	0.66	98.26	67	839	1.64
HY7a	2rim	47.67	1.54	9.45	0.13	11.35	0.08	14.20	11.08	1.51	0.72	97.73	69	840	2.07
HY7a	4core	42.48	1.16	12.94	0.04	12.10	0.16	12.12	12.04	1.40	1.80	96.24	64	955	4.34
HY7a	4rim	45.10	1.06	11.82	0.18	11.57	0.15	13.57	11.02	1.39	1.55	97.41	68	900	3.77
HY10	1core	45.14	2.03	9.81	0.00	14.05	0.18	11.95	10.82	1.56	0.91	96.46	60	855	2.17
Biotite		wt%													
Sample	Point	SiO_2	TiO_2	Al_2O_3	Cr_2O_3	FeO	MnO	MgO	CaO	Na_2O	K_2O	total	Mg#	T(°C)	texture
HY1	1core	34.14	4.85	18.86	0.00	23.15	0.11	6.35	0.00	0.36	9.03	96.84	33	729	subhedral
HY1	1rim	34.13	4.44	18.31	0.00	22.85	0.10	6.19	0.02	0.68	8.87	95.58	33	719	subhedral
HY1	2core	34.57	4.01	18.65	0.00	21.98	0.16	5.76	0.16	0.45	8.91	94.64	32	704	subhedral
HY1	2rim	33.96	4.40	18.19	0.00	23.46	0.16	6.35	0.09	0.60	8.73	95.93	33	717	subhedral
HY1	3core	35.22	4.92	15.72	0.00	20.44	0.01	9.33	0.01	0.50	9.24	95.38	45	744	euhedral
HY1	3rim	36.49	4.57	15.47	0.04	19.81	0.09	9.68	0.00	0.33	9.21	95.68	47	735	euhedral
HY1	4core	34.77	4.80	18.23	0.00	22.68	0.02	6.21	0.01	0.76	8.87	96.36	33	728	rounded
HY1	4rim	33.44	4.49	18.82	0.01	22.22	0.00	5.97	0.06	0.62	9.06	94.67	32	721	rounded
HY1	5core	34.72	4.27	19.06	0.02	22.12	0.00	6.16	0.00	0.61	8.77	95.72	33	712	rounded
HY1	5rim	34.86	4.76	18.88	0.00	22.55	0.19	6.27	0.00	0.88	8.87	97.26	33	726	rounded
HY2	1core	35.33	4.81	18.87	0.02	23.37	0.01	6.38	0.00	0.55	8.66	97.99	33	726	rounded

Table 4 (*continued*)

Sample	Point	SiO_2	TiO_2	Al_2O_3	FeO	MnO	MgO	CaO	Na_2O	K_2O	total	Mg#			
HY2	2core	35.55	4.82	18.28	0.02	17.45	0.01	10.08	0.06	0.38	9.16	95.82	51	747	suhedral
HY2	3rim	38.39	5.40	15.72	0.02	16.10	0.21	13.34	0.02	0.53	9.16	98.89	59	772	euhedral
HY2	4core	35.89	4.78	18.46	0.00	18.78	0.08	10.28	0.05	0.52	8.88	97.72	49	741	subhedral
HY2	5core	35.41	4.58	19.10	0.04	22.88	0.00	6.23	0.00	0.38	8.19	96.81	33	720	rounded
HY6	1core	36.13	4.04	16.46	0.00	18.02	0.07	11.82	0.03	0.41	8.80	95.77	54	731	euhedral
HY6	1rim	36.72	4.81	16.12	0.06	17.08	0.05	11.65	0.01	0.49	8.95	95.93	55	754	euhedral
HY6	2core	34.33	4.74	18.82	0.07	23.20	0.07	6.54	0.01	0.53	9.15	97.45	33	726	subhedral
HY6	2rim	34.03	4.70	18.43	0.04	22.15	0.03	6.97	0.00	0.60	8.93	95.87	36	728	subhedral
HY6	3core	34.65	4.78	18.58	0.00	22.84	0.12	6.42	0.01	0.39	9.00	96.80	33	727	subhedral
HY6	3rim	35.10	4.90	18.91	0.06	22.60	0.10	6.32	0.00	0.29	9.22	97.50	33	729	subhedral
HY7a	1core	34.93	4.30	18.96	0.03	23.51	0.10	5.62	0.00	0.68	9.46	97.59	30	710	subhedral
HY7a	1rim	34.29	4.16	18.73	0.00	22.23	0.08	6.10	0.00	0.51	9.40	95.51	33	710	subhedral
HY7a	2core	34.72	4.47	18.20	0.00	23.36	0.08	6.18	0.00	0.61	9.12	96.76	32	718	rounded
HY7a	2rim	34.63	4.50	18.76	0.10	22.34	0.04	6.23	0.01	0.60	9.20	96.40	33	719	rounded
HY7a	3core	34.67	4.15	17.49	0.03	19.14	0.10	9.02	0.01	0.38	9.47	94.47	46	723	euhedral
HY7a	4core	34.23	4.90	18.41	0.03	21.53	0.10	6.20	0.00	0.60	9.06	95.06	34	733	rounded
HY7a	5core	34.46	4.14	18.05	0.00	19.69	0.06	9.09	0.02	0.55	9.09	95.15	45	721	euhedral
HY7a	6core	35.75	4.51	18.43	0.02	21.56	0.10	6.08	0.03	0.43	8.82	95.72	33	720	rounded
HY7b	2core	35.98	4.29	16.14	0.01	21.39	0.03	8.00	0.08	0.31	9.24	95.46	40	720	euhedral
HY7b	2rim	35.45	3.83	16.96	0.00	21.67	0.08	8.08	0.06	0.32	9.34	95.79	40	704	euhedral
HY7b	5core	36.50	4.39	15.67	0.08	15.40	0.13	13.35	0.06	0.47	8.84	94.90	61	756	subhedral
HY7b	5rim	37.35	4.05	15.00	0.04	13.99	0.08	13.15	0.09	0.43	8.45	92.62	63	752	subhedral
HY7b	6rim	36.03	4.34	16.40	0.11	16.51	0.00	11.62	0.02	0.70	9.32	95.05	56	744	euhedral
HY7b	mafic inc.gm 1core	37.96	4.68	15.82	0.21	13.80	0.00	13.50	0.03	0.65	8.64	95.29	64	768	acicular
HY8	2core	35.13	4.97	18.57	0.04	23.10	0.05	6.21	0.01	0.31	9.15	97.54	32	731	rounded
HY8	3core	35.20	4.20	18.66	0.01	22.29	0.03	6.27	0.04	0.36	8.71	95.75	33	710	rounded
HY8	5core	36.46	4.33	17.44	0.06	15.34	0.12	9.89	0.17	0.40	8.03	92.23	53	741	euhedral
HY8	5rim	36.82	4.08	16.89	0.07	15.90	0.08	10.12	0.15	0.41	7.50	92.01	53	733	euhedral
HY9	1core	34.47	4.80	18.39	0.00	22.25	0.05	6.59	0.00	0.50	9.25	96.30	35	729	suhedral
HY9	4core	34.41	4.89	18.30	0.04	23.50	0.06	6.49	0.00	0.66	9.44	97.78	33	730	rounded
HY9	5core	34.02	4.79	18.86	0.03	22.91	0.03	6.35	0.02	0.53	9.63	97.17	33	728	rounded
HY9	5rim	34.13	4.81	18.36	0.07	23.34	0.02	6.32	0.04	0.47	8.86	96.43	33	728	rounded
HY9	6core	33.80	4.80	18.22	0.02	22.59	0.08	6.27	0.08	0.40	8.94	95.19	33	730	rounded
HY9	6rim	35.33	4.17	18.58	0.01	21.51	0.00	6.51	0.06	0.47	8.48	95.12	35	711	rounded
HY9	mafic inc.gm 1core	35.06	4.60	19.35	0.01	20.62	0.06	7.92	0.02	0.67	8.63	96.93	41	727	interstitial
HY10	1core	36.71	4.16	19.11	0.03	22.96		6.55		0.38	9.23	99.12	34	704	rounded
HY10	3core	36.71	4.78	15.34	0.07	16.26	0.13	12.56	0.03	0.49	9.26	95.62	58	760	euhedral
HY10	3rim	37.54	4.52	15.82	0.02	15.88	0.02	12.26	0.02	0.40	9.30	95.78	58	752	euhedral
HY10	5core	35.84	4.37	18.62	0.04	21.16	0.03	6.28	0.06	0.32	8.68	95.40	35	716	rounded
HY10	6core	34.90	4.59	18.51	0.06	20.60	0.03	6.50	0.02	0.44	9.13	94.77	36	725	rounded
HY10	6rim	34.83	4.80	18.57	0.00	22.18	0.09	6.53	0.00	0.53	8.91	96.44	34	729	rounded
HY10	inc. clot 1core	39.18	4.03	15.91	0.05	11.05	0.06	16.57	0.02	0.44	9.02	96.33	73	773	subhedral
HY10	inc. clot 1middle1	36.48	5.08	15.67	0.03	14.43	0.00	14.40	0.03	0.44	8.80	95.36	64	780	subhedral
HY10	inc. clot 1middle2	36.22	4.14	16.01	0.02	18.08	0.12	12.22	0.00	0.42	8.75	95.99	55	735	subhedral

Inc. clot, clot type inclusion; mafic inc., mafic inclusion; Mg#, 100*[Mg/(Mg + Fe)]; T, temperature. Thermobarometric results in the amphibole and biotite phenocrysts are from Ridolfi and Renzulli (2012), and Henry et al. (2005), respectively.

Table 5
Representative chemical compositions (wt%) of spinel, cordierite, ilmenite and garnet xenocrysts compared with data from previous studies in the crustal xenoliths embedded in the lava samples of El Hoyazo.

Sample	Mineral	SiO_2	TiO_2	Al_2O_3	Cr_2O_3	FeO	MnO	MgO	CaO	Na_2O	K_2O	Total
HY8	ilm	0.06	53.89	0.13	0.00	45.63	0.20	1.09	0.03	0.00	0.04	101.07
AV 07	ilm	0.00	53.65	0.17	0.06	44.71	0.80	0.40	0.00	0.00	0.02	99.81
HY9b	grt	37.67	0.00	21.92	0.00	34.44	2.66	2.65	1.84	0.03	0.03	101.24
AV 07	grt	37.62	0.06	21.09	0.00	37.18	0.57	3.63	1.20	0.00	0.02	101.37
AV 07	grt	37.41	0.00	20.75	0.01	37.06	0.62	3.77	1.27	0.00	0.01	100.90
AV 07	grt	37.92	0.02	20.92	0.08	34.23	2.63	3.51	1.29	0.00	0.03	100.63
HY2	spl	0.00	0.16	62.88	0.01	30.63	0.26	7.78	nd	nd	nd	101.72
HY2	spl	0.00	0.18	62.52	0.03	30.25	0.36	8.10	nd	nd	nd	101.44
AV-K 10	spl	0.06	0.27	56.12	na	39.19	0.38	2.86	nd	nd	nd	98.88
AV-K 10	spl	0.00	0.29	59.61	na	33.68	0.51	6.85	0.02	nd	0.01	100.97
AV-K 10	spl	0.06	0.53	57.51	na	36.98	0.39	3.81	nd	nd	0.01	99.29
AV-K 10	spl	0.07	0.42	55.55	na	40.29	0.33	2.40	0.02	0.01	nd	99.09
HY7a	crd	49.13	0.10	34.26	0.01	8.12	0.04	8.47	0.38	0.30	0.22	101.03
HY7a	crd	49.47	0.13	33.47	0.02	11.21	0.09	6.26	0.18	0.09	0.10	101.02
HY7a	crd	49.39	0.00	33.90	0.00	7.31	0.21	9.27	0.12	0.15	0.22	100.57

(*AV 07*: Álvarez-Valero et al., 2007; *AV-K 10*: Álvarez-Valero and Kriegsman, 2010).

Table 6
Whole-rock compositions (major and trace elements) of the studied lava samples. $Fe_2O_3^*$, total iron calculated as F_2O_3.

Sample	SiO_2	TiO_2	Al_2O_3	$Fe_2O_3^*$	MnO	MgO	CaO	Na_2O	K_2O	P_2O_5	total	V	Cr	Ni	Cu	Zn	Rb	Sr	Y	Zr	Nb	Ba
HY7aW	61.45	0.681	16.97	5.71	0.055	2.80	3.15	1.96	2.99	0.179	95.95	127.2	90.1	32.8	38.4	74.8	129.7	420	27.1	200	14.9	578
HY7aD	63.25	0.645	16.38	5.29	0.049	2.19	2.69	2.06	3.25	0.175	95.98	121.1	92.9	35.9	51.0	90.4	143.3	398	26.8	199	15.9	637
HY1aW	61.86	0.675	16.81	5.69	0.076	2.69	3.29	1.96	3.10	0.191	96.34	125.7	99.5	33.5	37.4	74.8	128.6	449	21.7	197	15.6	562
HY1aD	61.88	0.676	17.84	5.42	0.056	2.07	2.58	2.06	3.48	0.186	96.25	117.2	82.2	31.0	33.5	71.1	139.5	421	21.1	188	15.3	590
HY7b	62.91	0.620	16.57	5.32	0.070	2.38	2.67	1.84	3.40	0.167	95.95	106.4	80.6	27.0	22.1	75.5	143.3	359	28.7	182	15.6	559
HY2	64.59	0.629	16.63	4.96	0.054	1.80	2.47	2.41	3.97	0.172	97.69	102.3	83.0	30.9	18.5	75.9	162.9	367	24.8	188	15.6	642
HY8a	63.87	0.572	16.55	4.80	0.060	2.20	2.75	2.02	3.64	0.142	96.60	104.3	75.1	25.7	23.6	75.8	144.6	363	24.1	185	14.8	538
HY9b	63.98	0.653	16.48	5.34	0.050	2.18	2.66	2.24	3.82	0.151	97.55	110.7	89.5	39.6	48.1	68.0	134.9	386	24.8	190	15.7	648
HY10	63.45	0.584	17.49	4.54	0.060	2.67	3.57	2.18	3.07	0.098	97.71	98.9	67.7	27.5	16.9	69.8	80.7	451	23.8	195	15.9	689

W, whiter part; D, darker part.

of the dacites (Table 1) reveals that plagioclase, biotite, and quartz are present in all samples, whereas amphibole and/or pyroxenes occurred in four samples (Table 1). All minerals can be subdivided into several types based on textural features (Figs. 2–6):

Plagioclase: according to the textural features of the core domains, plagioclase phenocrysts can be grouped into four main types (Fig. 3): (a) anhedral to subhedral homogeneous core type lacking obvious compositional zoning in core; (b) euhedral to subhedral oscillatory zoning type; (c) euhedral to subhedral patchy type characterized by An-poor areas within an An-rich main crystal, (d) euhedral to subhedral resorbed type containing abundant glass inclusions with local oval holes in the core. The patchy and resorbed types show a normally zoned outer core to rim, whereas the homogeneous core type and oscillatory zoning type show normal or reverse zonation at the rim. Sieve textures are locally observed in the outer core of the patchy type and in between core and rim of the homogeneous core type. The four types normally coexist. Locally, homogeneous core type plagioclase is enclosed by biotite phenocrysts.

Hornblende can be divided into (i) euhedral (HY1), (ii) subhedral (HY6), and (iii) opacite rim types (rest of samples) (Fig. 4). Opposite to the plagioclase cases, hornblende types are not combined within the same sample.

Pyroxene: ortho- and clinopyroxene phenocrysts mostly occur in samples HY7a, HY7b and HY10, showing either sieved (in the rims) or subhedral textures (Fig. 5). Locally orthopyroxene is enclosed by biotite phenocrysts.

Biotite shows euhedral, subhedral, and rounded shapes (Fig. 6).

Quartz phenocrysts and large xenocrysts are generally (sub)rounded (Fig. 2c–d).

Dacites also enclose xenocrysts of euhedral garnet (HY9b), anhedral ilmenite (HY8a), spinel (HY2) and euhedral cordierite (HY7a).

Magmatic crystal aggregates, as enclaves or pockets in the dacite groundmass, are also common, grouped in two main types: (i) the mafic inclusion: diktytaxitic textures composed of acicular to columnar plagioclase with interstitial gas bubbles (e.g., HY7b, HY9b; Fig. 7a–b); (ii) the clot type inclusion: cumulophyric textures showing crystal

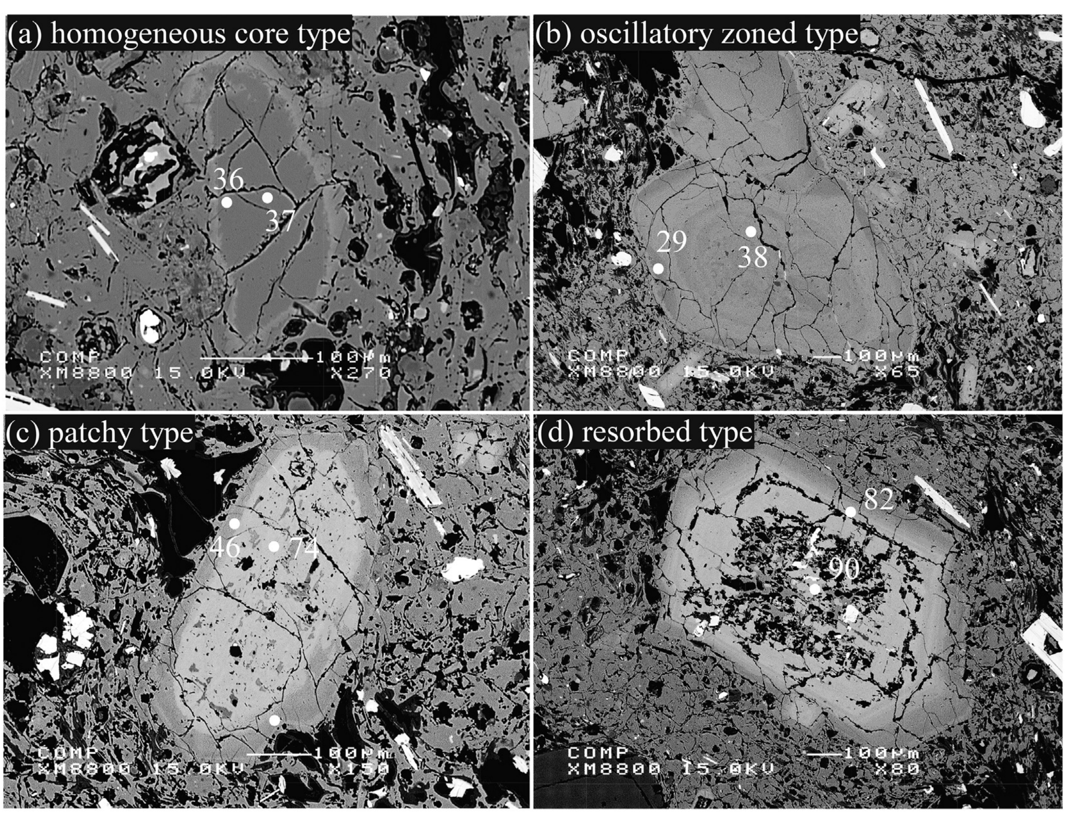

Fig. 3. Back-scattered electron images of representative plagioclase phenocrysts and An content of the four main types. In (a) phenocryst shows a thin resorption rim. See main text for details.

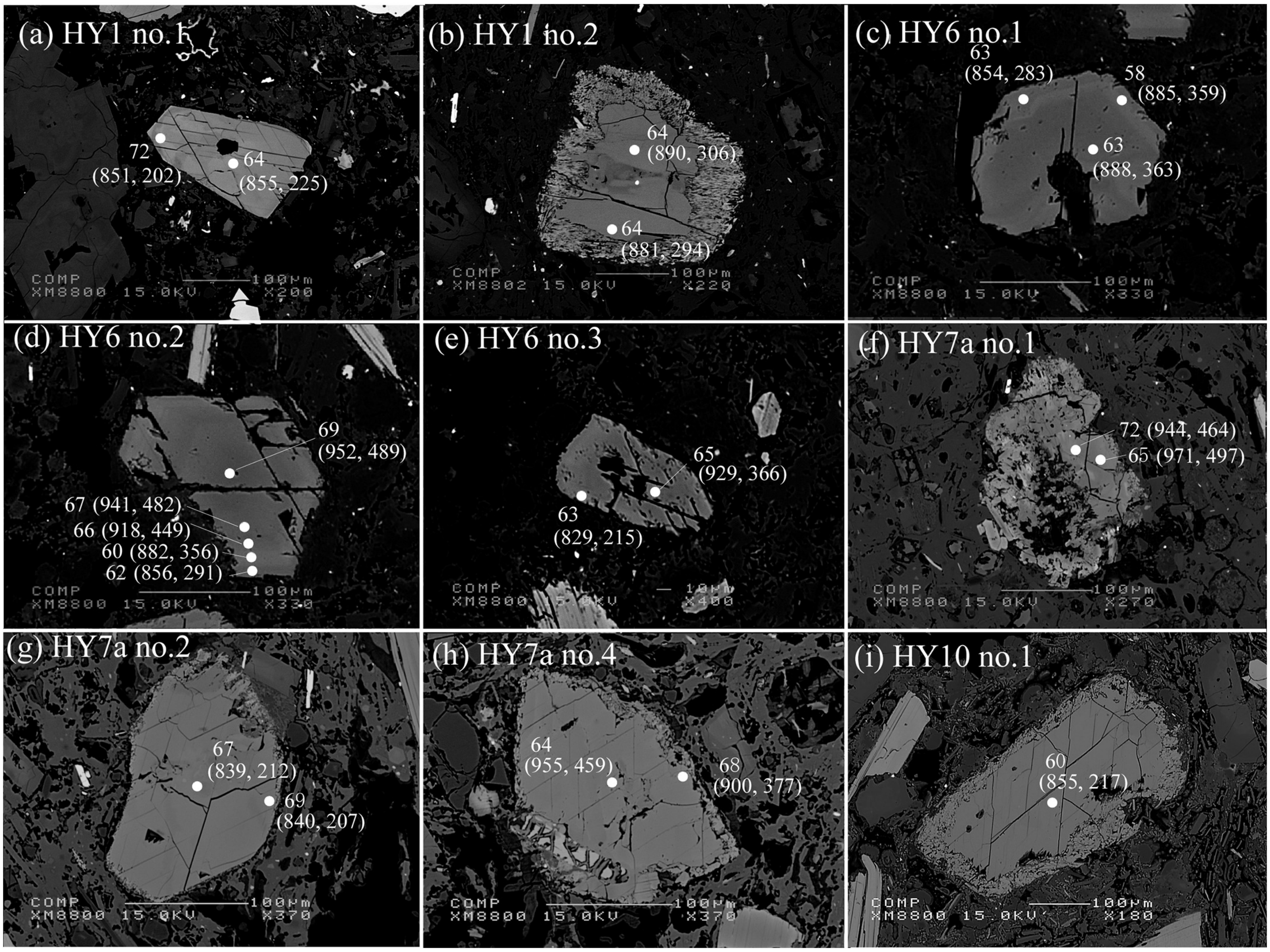

Fig. 4. Back-scattered electron images and Mg# values of hornblende phenocrysts (T estimates). See main text for details.

clots of orthopyroxene microlites with local plagioclase, biotite, and isolated orthopyroxene phenocrysts with strong normal zoning (e.g., HY1, HY10; Fig. 7c–d). Interstitial glass is also present, which shows a rhyolitic composition ca. 74% SiO_2. Local orthopyroxene clot grains (e.g., HY10) are partly enclosed by biotite, intergrown with a plagioclase phenocryst. In addition, a crystal aggregate pocket of plutonic origin in HY1 and HY2 (ca. 2 mm in diameter) shows equigranular texture, composed of anhedral hornblende and quartz, anhedral to subhedral plagioclase, and subhedral biotite, and is progressively disaggregated toward the outer parts.

The estimation of the phenocryst modal abundances (image analysis using Photoshop and ImageJ) reveals that plagioclase and biotite together account for 9.9–16.5 vol% (Table 2). The modal abundance is not clearly correlated with sample appearance (groundmass general colour, i.e., darker or lighter). Hence, the dark colour may have another origin, such as finely dispersed iron-titanium oxides. Quartz is present in all samples, but its modal content is mostly lower (1.0–6.3%) than that of plagioclase and biotite. Pyroxene and amphibole phenocrysts are minor phases (< 1%). Large garnet xenocrysts are locally present, accounting for up to 3.8% in HY9b.

3.2. Mineral chemistry

Tables 3 and 4 contain representative compositions of plagioclase, orthopyroxene, biotite and amphibole phenocrysts. Histograms of anorthite content (An%) in plagioclase show a wide variation from 27% to 90% depending on the plagioclase type (Fig. 8). The homogeneous core type shows a core with $An_{30–50}$ and a rim of An_{40-60}. The core composition of the oscillatory type is in the range of $An_{38–74}$ (light zones) and An_{27-61} (dark zones) with rims around An_{40-60}. Chemically, this type can be divided into low An ($An_{ca.30–50}$) and intermediate An ($An_{ca.50–70}$). The crystals showing lower An in dark zones also show lower An in light zones, and vice versa. The patchy type core composition is An_{64-84}, with rims around An_{50}. The resorbed type has core composition of An_{77-90} with rims around An_{45-60}. The core composition of plagioclase in the diktytaxitic magmatic and orthopyroxene clot inclusion types is ca. An_{76} and $An_{85,}$ respectively, with rims of ca. An_{50} (Fig. 8). One tiny plagioclase enclosed by a biotite phenocryst in sample HY7b has ca. An_{50} in the core. Reverse zoning in plagioclase can in some cases be an additional sign of partial melting (e.g., Álvarez-Valero and Kriegsman, 2010).

The composition of hornblende phenocrysts ranges from pargasitic-, tschermakitic- to magnesio-hornblende in samples HY6 and HY7a. The latter is near the boundary between the two hornblende types, yet within the subhedral type. Except for one grain in HY1 (euhedral type), all magnesio-hornblende phenocrysts in HY1a and HY10 belong to the opacite rim type (Fig. 9).

Ortho- and clinopyroxene phenocrysts show the Mg-richer parts distributed irregularly from rim to core. For instance, phenocrysts in HY7a (subhedral type) are heterogeneous, showing [Mg# = MgO/

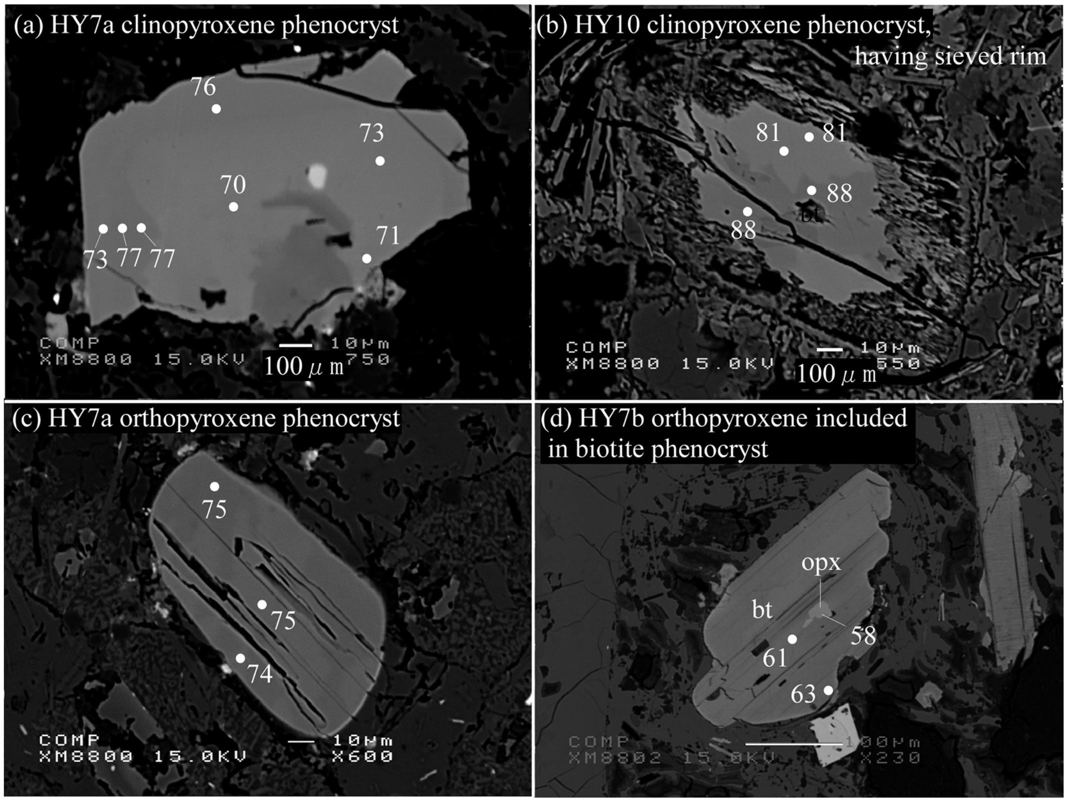

Fig. 5. Back-scattered electron images and Mg# values of clinopyroxene and orthopyroxene phenocrysts, and orthopyroxene included in a biotite phenocryst. See main text for details.

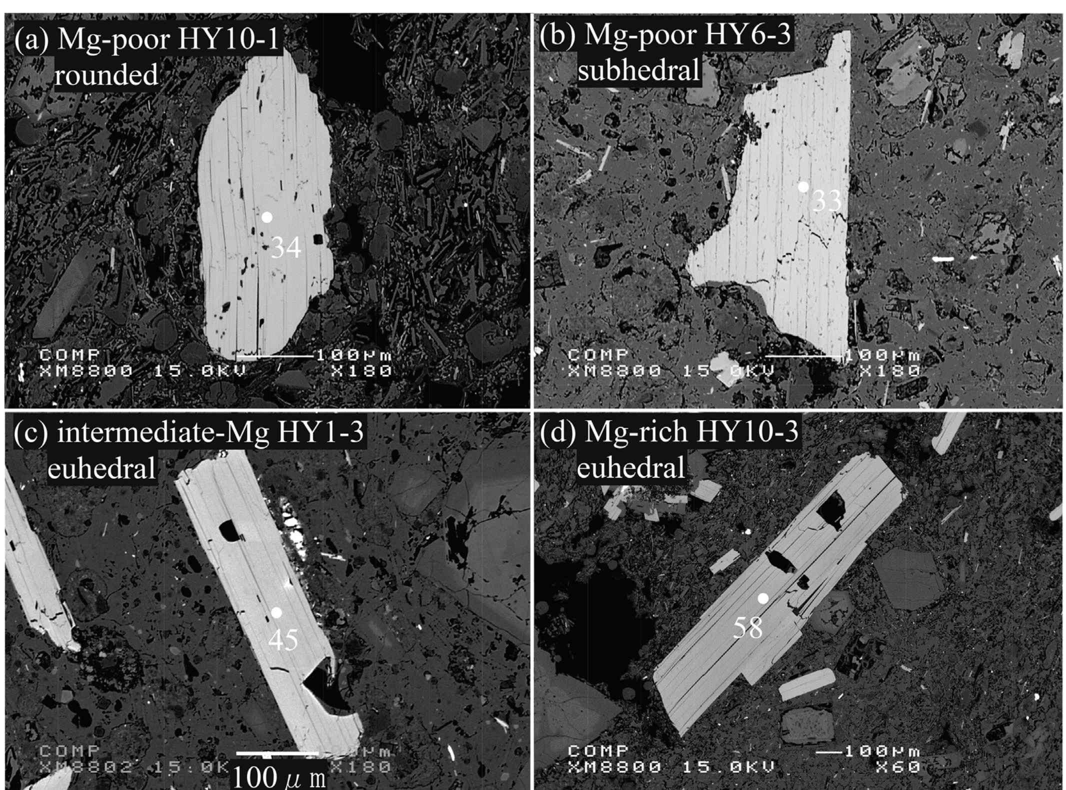

Fig. 6. Back-scattered electron images and Mg# values of biotite phenocrysts. See main text for details.

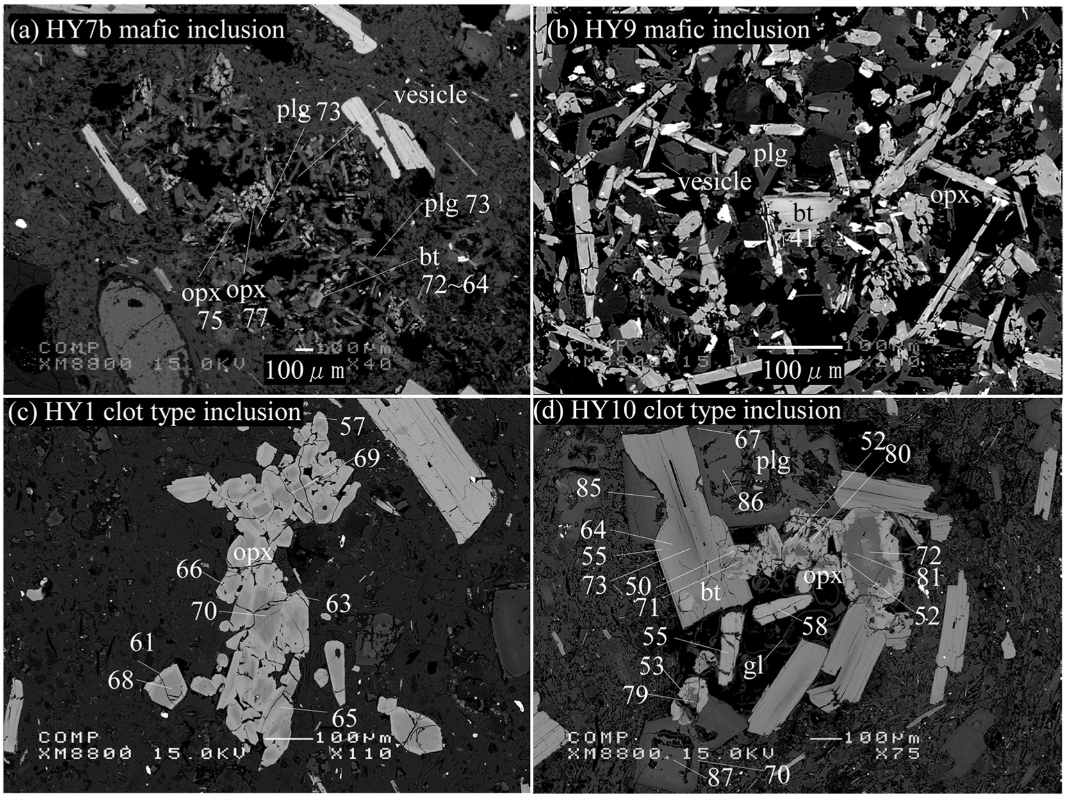

Fig. 7. Back-scattered electron images of clot type and mafic inclusions: plg, plagioclase; opx, orthopyroxene; bt, biotite; gl, glass; numbers correspond to An content in plagioclase and Mg# values for the rest. See main text for details.

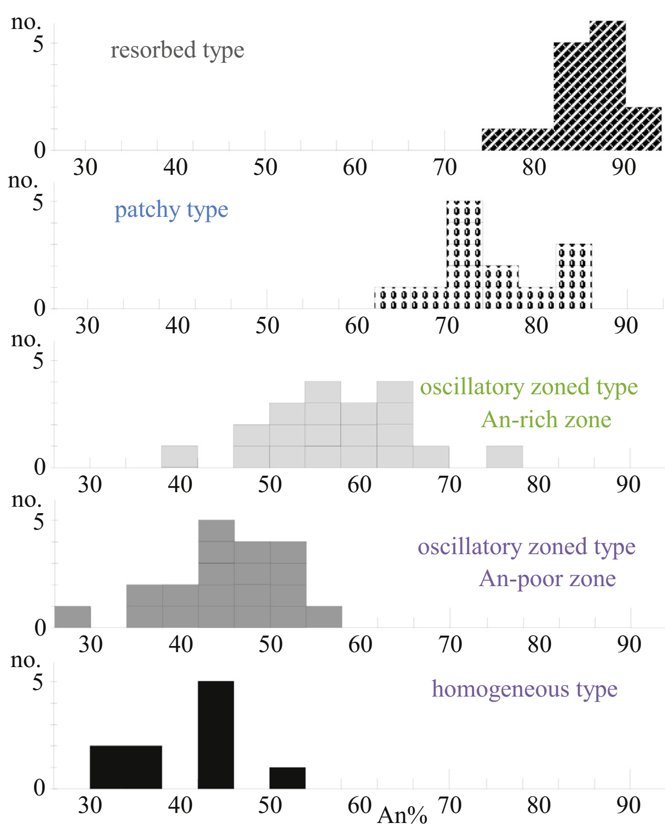

Fig. 8. Histograms of anorthite (An) content of plagioclase phenocrysts.

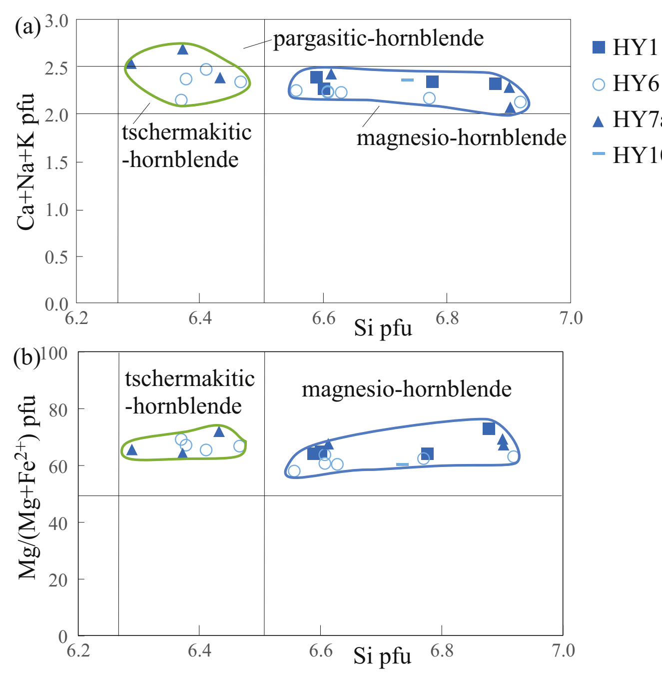

Fig. 9. (a) (Ca + Na + K) vs. SiO_2 diagram of amphibole phenocrysts. Division lines from Leake (1968); (b) Mg# value vs. SiO_2 diagram of amphibole phenocrysts.

(MgO + FeO)] 74–75 (orthopyroxene) and 70–77 (clinopyroxene) (Fig. 5). Clinopyroxene of the sieved type has compositionally heterogeneous core parts in the range of Mg# 80–88. Orthopyroxene crystals in the clot inclusions show normal zoning with higher Mg# in the core than in the rims, except for one grain in HY10, which has a lower Mg# of 72 in the core (Fig. 7). In sample HY1 the Mg# ranges from 57 to 70, and from 50 to 81 in HY10. The Mg# of the orthopyroxene inclusion in biotite is 58. Garnet, cordierite, ilmenite and spinel xenocrysts show compositions similar to those in the crustal xenoliths (e.g., Álvarez-Valero et al., 2007).

Biotite phenocryst compositions are Mg# ~40 for the Mg-poor group, 45–56 in the intermediate-Mg group, and higher than 58 for the Mg-rich group (Figs. 6 and 10). Most of the Mg-poor group are rounded, whereas most of the intermediate and Mg-rich groups show subhedral to euhedral shapes. Silicon mostly ranges from 5.3 to 6.0 (Si apfu) and shows a slightly negative correlation with Mg# (Table 4), probably due to Mg-Tschermak substitution. Biotite cores (phlogopite) showing normal zoning (Fig. 10) in the clot inclusion type have Mg# ~73. The acicular crystals in the mafic inclusions have Mg# ~72. One interstitial small biotite in a mafic inclusion of sample HY9 shows Mg# 41 (Fig. 7).

3.3. Geochemistry

XRF whole rock analyses of 9 samples (all except HY6) are normalized to 100% volatile free with total iron (FeO*) calculated as FeO (Table 6; Figs. 11–12). All samples belong to the high-K, calc-alkaline series (Gill, 1981). A/CNK = 1.8 ± 0.1, i.e., highly peraluminous (Shand, 1943). Major oxide and trace element variation diagrams show a similar trend (Fig. 11). Na_2O and K_2O increase slightly with increasing SiO_2 content, whereas Al_2O_3, FeO*, MgO, CaO, P_2O_5, Cu, Ni, Zr and Cr decrease with respect to SiO_2. TiO_2, Rb, Nb and Y concentrations are fairly constant, independent of SiO_2. Sample HY10 deviates in showing higher CaO and Ba, and lower FeO*, P_2O_5, Rb, V and Cu contents than the average trend line (Fig. 11). Normally, the darker bands display higher SiO_2 content than the lighter ones, yet HY1 and HY7a are different: e.g., HY1D is slightly apart from the general trend in Al_2O_3 and MgO content (Fig. 11).

In the diagrams normalized to primordial mantle (Fig. 12a) El Hoyazo dacites show patterns very close to average upper crust. This pattern matches a subduction origin that is characterized by high K,

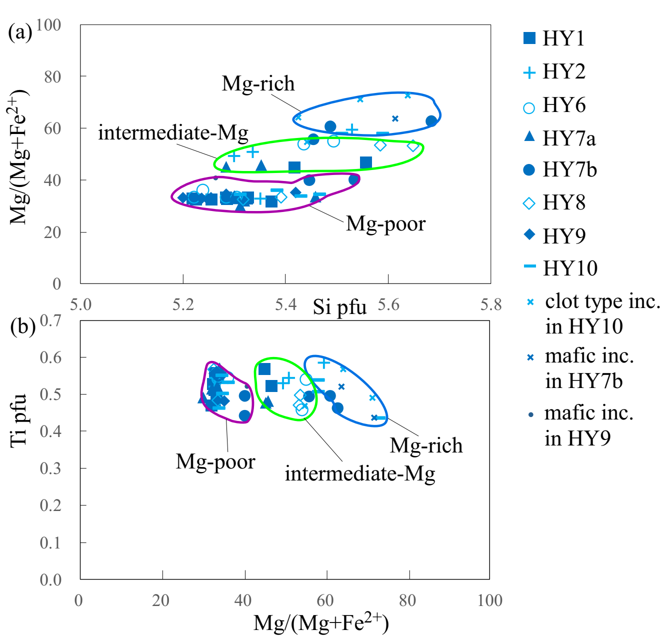

Fig. 10. (a) Mg# value vs. SiO_2 and (b) Ti vs. Mg# diagrams of biotite phenocrysts. See details in the text about the different biotite types.

Rb, and Ba (LILE) concentrations and depletion of P and Ti. In the discrimination diagrams of felsic rocks the samples plot within the areas of volcanic arc (Fig. 12b) and volcanic arc plus *syn*-collision (Fig. 12c) settings. This is also consistent with the geological origin of El Hoyazo volcano, related to the convergent margin of the European-African plate collision and subduction zone (e.g., García-Dueñas et al., 1992; Vissers et al., 1995). The data also show a clear negative Nb anomaly (Fig. 12a), which is typical for magmas derived by subduction-related melting of the mantle wedge in supra-subduction zone settings (Gill, 2010).

The results of oxygen and hydrogen stable isotope analysis (Table 7; Fig. 13) in amphibole, plagioclase + quartz, and whole rock samples show higher $\delta^{18}O$ values (12.5 to 15.6‰) than MORB values (5–6‰) and arc volcanoes (5–8‰), within the range of metamorphic rocks (Bindeman, 2008), which fits partial melting of crustal material. D/H results for quartz + plagioclase and for whole-rock display a wide range of values with no particular systematics, yet within the range of metamorphic and sedimentary fluids (Fig. 13).

3.4. P-T conditions

Biotite T estimates (Henry et al., 2005) indicate 704–733 °C, 721–754 °C and 756–770 °C, for Mg-poor, intermediate-Mg- and Mg-rich phenocrysts, respectively. For the acicular and interstitial crystals in mafic pockets, the retrieved T is ca. 770 °C and 727 °C, respectively, whereas the biotite core (phlogopite) in the clot inclusion type gives 773 °C. The two-pyroxene thermobarometer (Putirka, 2008; eq. 36 and 39), applied to the Mg-poor and Mg-rich parts of ortho- and clinopyroxene pairs in sample HY7a, indicate 776–813 °C, 1.7–1.9 kbar, and 822 °C, ca. 2.2 kbar, respectively. Regarding the P-T results for amphiboles (Ridolfi and Renzulli, 2012), the subhedral type gives values of 3.6–4.9 kbar, 888–952 °C for the phenocryst cores and 2.2–2.9 kbar, 829–856 °C for the rims. Both core and rim of the euhedral type and two cases of the opacite rim type show lower P-T conditions than the previous type at 2.0–2.3 kbar and 839–855 °C. By contrast, the rest of the opacite rim type gives higher *P* values of 3.1–5.0 kbar at 890–971 °C for the cores, with outer cores at lower P values of 2.9–3.8 kbar at 881–900 °C. These data are interpreted in terms of a relatively stable magma chamber at shallower level than ~6–7.5 km, and influx of magma batches from ~15 km depth (Fig. 15) where most of the restites were incorporated into the ascending magma (e.g., Álvarez-Valero et al., 2016).

4. Discussion

4.1. Magma mixing beneath El Hoyazo

Our petrological and geochemical results reveal mixing processes of magmas, mainly evidenced by the presence of (i) microdomains of a hotter magma enclosed by (i.e., quenched within) the lower-T dacites; (ii) banded (dark vs light) textures; (iii) coexisting disequilibrium phenocrysts (i.e., quartz and biotite vs. An-rich plagioclase and Mg-rich pyroxenes); (iv) a wide range of An content among the plagioclase phenocrysts; (v) orthopyroxene clot grains enclosed by biotite overgrowing on a plagioclase phenocryst indicate that the core of orthopyroxene and plagioclase crystallized from a hotter magma, whereas its zoned parts formed subsequently from a cooling and differentiating magma.

Modal amounts of phenocrysts indicate that more than 99% are biotite, plagioclase, and quartz. Based on their chemical compositions (Figs. 8 and 10), biotite and plagioclase compositions can be divided into relatively high-T and low-T varieties. The equilibrium phenocryst assemblage consisting of An-poor plagioclase (homogeneous core type) + Mg-poor biotite + quartz suggests formation from high-SiO_2 dacitic or rhyolitic magma. By contrast, the phenocryst assemblage of intermediate-An plagioclase (An intermediate oscillatory zoned type

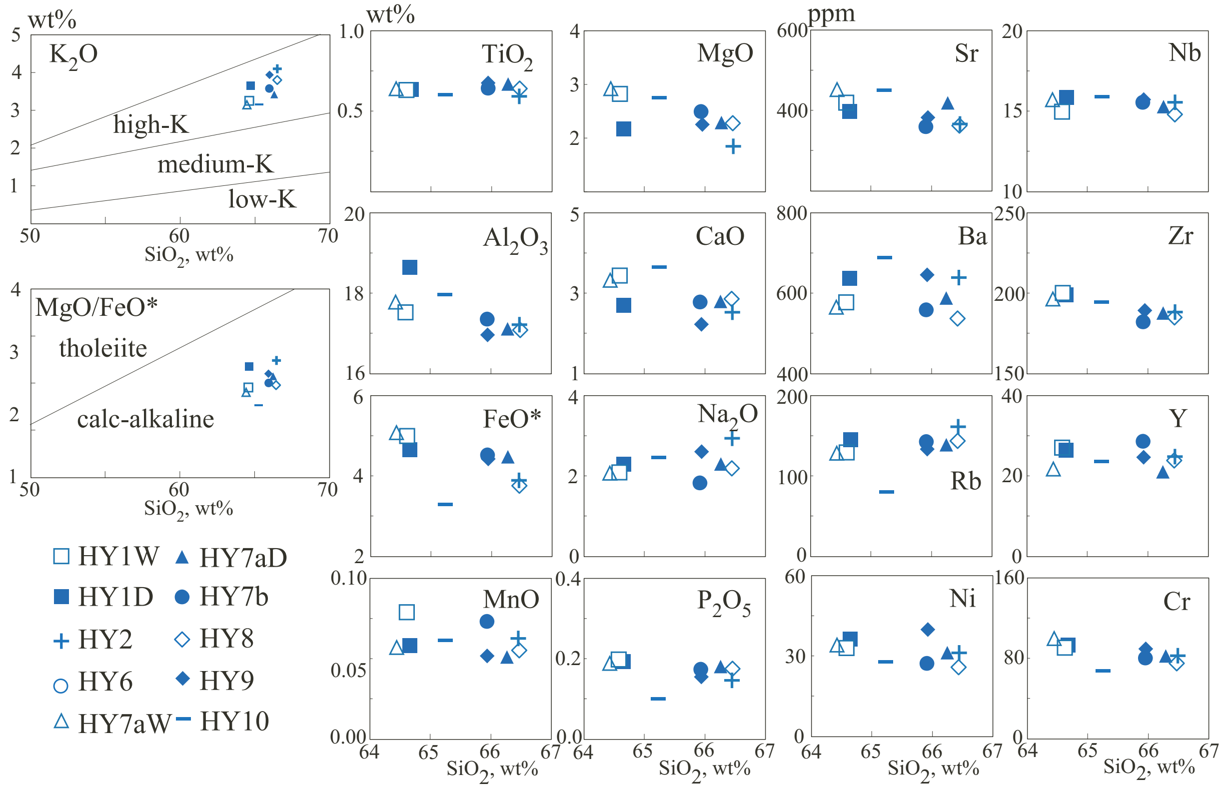

Fig. 11. Major and trace elements vs. SiO_2 variation diagrams of the studied lava samples. FeO* is total iron calculated as FeO. Division lines in K_2O vs. SiO_2 diagram are from Gill (1981). The boundary line in FeO*/MgO vs. SiO_2 diagram is from Miyashiro (1974).

and intermediate-An patchy zoned type) and intermediate-Mg biotite (with or without quartz) suggests formation from high-SiO_2 andesitic or low-SiO_2 dacitic magma. The oscillatory zoning plagioclase type can be divided in two subgroups: (a) phenocrysts with $An_{ca.50–70}$ may have formed in the high-SiO_2 andesitic magma chamber, and (b) phenocrysts with $An_{ca.30–50}$ may have formed in the low-SiO_2 dacitic magma chamber. The oscillatory zoning results from multiple injections leading to mixing and subsequent convection. Hence, El Hoyazo dacites can be explained mainly by mixing of these two end-member magmas. The subordinate Mg-rich biotite group and the An-rich (resorbed type and patchy zoned type) plagioclase groups point to a low-SiO_2 magma (andesite or basaltic) from deeper parts. Yet, it had no significant

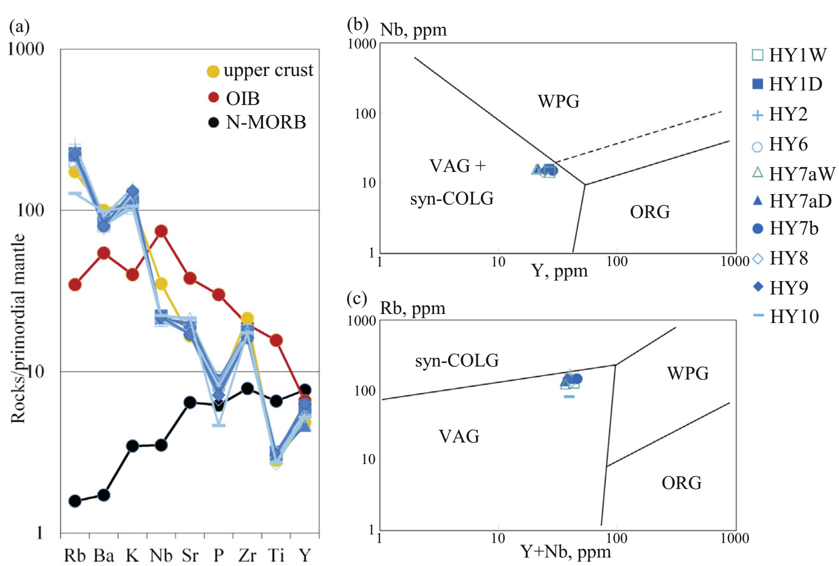

Fig. 12. (a) Trace element concentrations normalized to the composition of the primordial mantle; and (b) Nb vs.Y and (c) Rb vs. Y + Nb discrimination diagrams (Pearce et al., 1984) of the studied lava samples. In (a), the elements are arranged from left to right in order of increasing compatibility in a small fraction melt of the mantle. The normalizing values are those of McDonough et al. (1992). The values of upper crust are taken from Weaver and Tarney (1984). The values for average N-type MORB (Mid-Ocean Ridge Basalt) and OIB (Oceanic Island Basalt) are taken from Saunders and Tarney (1984) and Sun (1980), respectively. In (b) and (c), the fields of volcanic-arc granites (VAG), *syn*-collisional granites (syn-COLG), within-plate granites (WPG) and ocean-ridge granites (ORG) and the dashed line of the boundary for ORG anomalous ridges are from Pearce et al. (1984).

Table 7
Oxygen and hydrogen stable isotope results (including H_2O content) in representative phenocrysts and whole-rock samples.

Sample	Type	$\delta^{18}O$ ‰	δD_{SMOW}, ‰	% H_2O
HY-1	Amph	13.4	−64.0	3.0
HY-10	Amph	12.5	−71.0	2.6
HY-12	Amph	12.8	−71.6	2.6
HY-2	Amph	13.4	−80.0	2.7
HY-6	Amph	12.4	−70.0	3.1
HY-7a	Amph	12.8	−73.2	3.0
HY-8a	Amph	13.3	−75.1	2.8
HY-1	Q-Pl	14.9	−36.5	0.9
HY-10	Q-Pl	13.8	−75.0	0.9
HY-12	Q-Pl	13.9	−75.5	0.9
HY-2	Q-Pl	14.7	−94.1	0.8
HY-6	Q-Pl	15.0	−81.7	1.0
HY-7a	Q-Pl	14.7	−69.6	0.8
HY-8a	Q-Pl	15.6	−61.5	0.6
HY-6	W.R.	15.5	−66.8	1.3
HY-14-10[a]	W.R.	15.6	−83.6	2.3
HY-14-2[a]	W.R.	14.3	−93.0	3.3
HY-14-3a[a]	W.R.	15.5	−85.2	3.9
HY-14-8a[a]	W.R.	15.3	−91.0	4.1
HY-14-9a[a]	W.R.	15.1	−88.5	2.5

Amph, amphibole; Q, quartz, Pl, plagioclase, W.R., whole rock.
[a] Data from Álvarez-Valero et al. (2016).

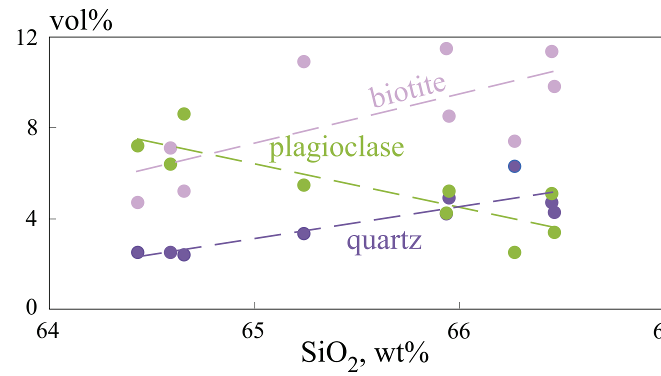

Fig. 14. Modal abundances of biotite, plagioclase, and quartz phenocrysts vs. SiO_2 content. Dashed lines correspond to regression trends, which have 95% confidence belts with a horizontal width of around ±2 wt%. More details in the text.

influence on the overall current lava composition. Plagioclase phenocrysts with An>80% suggest that the mafic magmas would correspond in composition to basaltic rather than andesitic.

The plagioclase modal content shows a linearly decreasing trend compared to the SiO_2 content, and the silica richer extension cuts the y-axis at ~67.5–68 wt% (Fig. 14). Here and below, the 95% confidence belt is around ±2 wt% (after the method of Davis, 2002, p. 202–203) Hence, given the presence of a small amount of An-poor plagioclase, the silicic end-member matches a high-SiO_2 dacitic or rhyolitic magma with ca. 68 wt% SiO_2. By contrast, the biotite modal abundance increases with SiO_2 content, showing ca. 14 vol% of biotite at 68 wt% SiO_2 (Fig. 14). The samples show an overall volume ratio between intermediate-Mg biotite, inferred to have crystallized from a more basic end-member, and Mg-poor biotite, derived from the more silicic end-member, of around 0.25. Thus, the more basic end-member may have contained ca. 3.5 vol% of biotite. In view of the biotite trend (Fig. 14), this implies ca. 62.5–63 wt% SiO_2. Consequently, El Hoyazo dacites reveal a mixing formation between high-SiO_2 andesitic and rhyolitic (or high-SiO_2 dacitic) magmas.

4.2. Mixing evidence of mafic magma from a deeper source

A direct evidence of magma mixing occurring beneath El Hoyazo volcano is the presence of relict inclusions of andesitic magma within a higher-SiO_2 lava host. This is further confirmed by: (i) the diktytaxitic texture that shows microlites with An-richer plagioclase within the groundmass than the phenocrysts in the host dacitic magma; this texture (e.g., HY7b, HY9b; Fig. 8a–b) is typical of quenched products of higher-T magma injected into a lower-T magma (e.g., Bacon, 1986); (ii) the orthopyroxene, biotite, and plagioclase crystals in the clot type inclusion showing strong compositional zoning toward the rim. Regarding the former (diktytaxitic texture), the An content of the acicular plagioclase (ca. ~75), and Mg# in cores of orthopyroxene and biotite (~77 and ~ 72, respectively) indicate precipitation from the basaltic

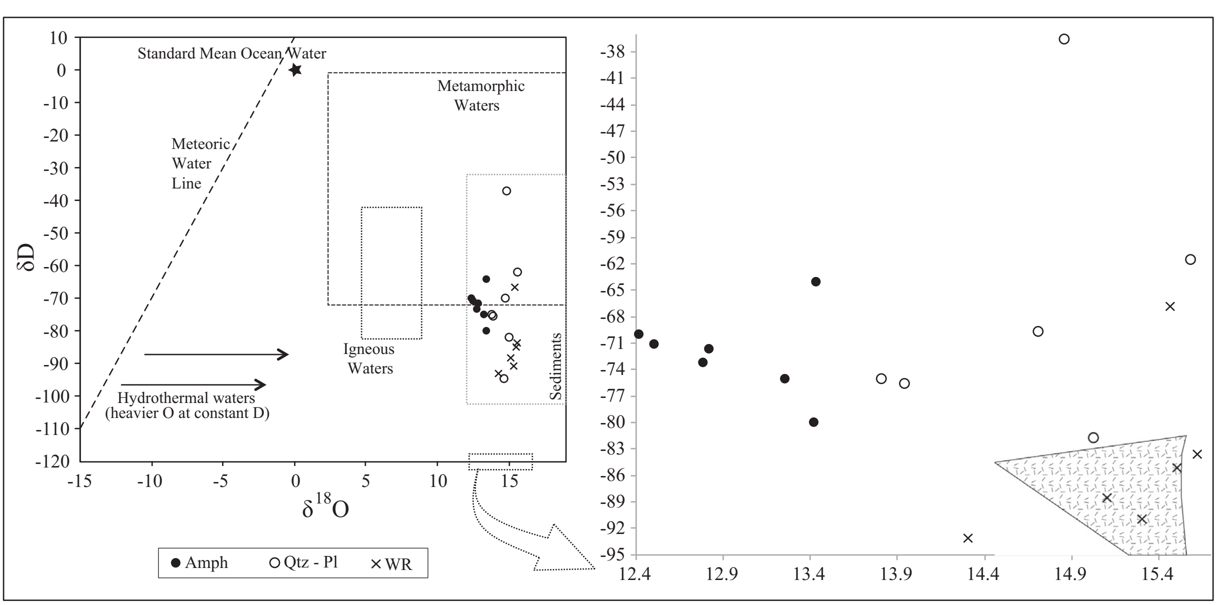

Fig. 13. (a) Representation of δD vs. $\delta^{18}O$ values (‰) of El Hoyazo lava samples in Taylor's (1967) diagram of water isotopic composition (Table 7). The temperature of the magmas (ca. 700–950 °C) did not allow for oxygen equilibration (typical at such high T) during rapid eruption, and therefore water δD reference values can be utilized for solid samples.

andesite magma. Concerning the orthopyroxene crystal clots, the maximum Mg# values of orthopyroxene and biotite (phlogopite) are 81 and 73, respectively. The biotite thermometer gives ca. 770 °C for phlogopite, which is higher than intermediate-Mg (ca. 750 °C) and Mg-poor (ca. 700–730 °C) biotites. In this clot type inclusion, the Mg# and An contents of orthopyroxene, biotite and plagioclase phenocrysts from core to rim are 81–50, 73–50 and 86–67, respectively. These phenocryst data describe a plumbing scenario in which their host magma arrived from deeper and hotter levels into the higher-SiO_2 magmas. As it cooled down the crystal cores of Mg-rich orthopyroxene and An-rich plagioclase precipitated, followed by the Mg-rich biotite (phlogopite), and finally by the lower Mg# and An outer cores and rims. In conclusion, these mafic and clot type inclusions represent the solidified products of the injected hotter magmas. The higher Al_2O_3 in the orthopyroxene core suggests a higher P origin (Table 4) of its parent magma.

$\delta^{18}O$ results reveal a clear metamorphic influence in all lava types and materials (whole rock and phenocrysts) from the partial crustal melting that produced the andesitic and dacitic mixed lavas (e.g., Álvarez-Valero et al., 2016; Benito et al., 1999; Cesare et al., 1997). Yet, hornblendes (lighter values than plagioclase, quartz and whole-rock samples) trend to a more primitive igneous component (Fig. 13). Phenocrysts show negligible $\delta^{18}O$ fractionation between dacites and included andesites, which is typical for rapid subvolcanic decompression occurring at high T (e.g., O'Neill, 1986).

Concerning D/H results, the wide range of values for plagioclase-quartz mixtures (Fig. 13) may be due to the influence of metamorphic material (see also Álvarez-Valero et al., 2016). The hornblende phenocryst and whole-rock of sample HY2 (having plutonic inclusion) match the lightest D/H values, i.e., nearest to the most primitive igneous signal.

4.3. Compositional heterogeneity of pyroxene phenocrysts

In the ortho- and clinopyroxenes, the Mg-richer parts are distributed irregularly within outer and inner parts, which could mean that the Mg-richer parts formed by the Fe-Mg inter-diffusion between Mg-poorer pyroxenes and Mg-richer surrounding mafic (basaltic) magmas injected from deeper levels (Fig. 5). By contrast, Fe-Mg inter-diffusion under "static conditions" in the magma reservoir would have resulted in systematic reverse zoning. The irregular distribution may have formed under near-liquidus conditions in a dynamic system of a deeper magma interacting with a shallower one. The sieved texture of clinopyroxene in HY10, as well as the partially rounded shapes of pyroxenes in HY7a also support this interpretation.

Based on Fe-Mg partitioning between biotite and orthopyroxene (Fonarev and Konilov, 1986; Sengupta et al., 1990), it is clear that most orthopyroxenes have never been in equilibrium with the Mg-poor and intermediate-Mg biotites observed in the same samples. In the temperature range 600–800 °C, orthopyroxene always has a lower Mg# value than co-existing biotite, and in the range 800–850 °C they are almost the same (K_D close to 1). In our samples, however, the Mg# values of orthopyroxene (Mg# >70) are in most cases much higher than those of biotite. One of the few exceptions is an orthopyroxene inclusion (Mg# = 59) in biotite (Mg# = 61 at the core, 63 at the rim), which gives a T estimate of ~800 °C (Bt core) or ~ 730 °C (Bt rim). Most other mineral pairs give unreasonable temperatures far in excess of 1000 °C. Hence, we conclude that the large majority of orthopyroxene phenocrysts show disequilibrium with biotite and have been derived from more basic magmatic (andesitic) components. Hence the Mg-poorer orthopyroxene domains (776–813 °C and 1.7–1.9 kbar; with Cpx) did not form from the described two main end-member magmas. Therefore, we interpret that a previous pulse of hotter and deeper magmas (transporting crustal restites upward) connected to higher-SiO_2 melts at shallower depths, partly differentiated to allow the formation of Mg-poorer pyroxenes. The Mg-rich biotite may have crystallized in equilibrium with the Mg-poorer Opx and Cpx. This leads to a plumbing scenario of a transient-state stratified magma reservoir composed of – from top to bottom – high-SiO_2-dacitic, high-SiO_2 andesitic, and andesite magmas at ca. 6–7.5 km depth.

4.4. Hornblende origin

P and T estimates for the opacite rim and euhedral types are in line with the retrieved values for the Mg-richer parts of the phenocrystic pyroxenes in HY7a (Table 4). This suggests a common magma source

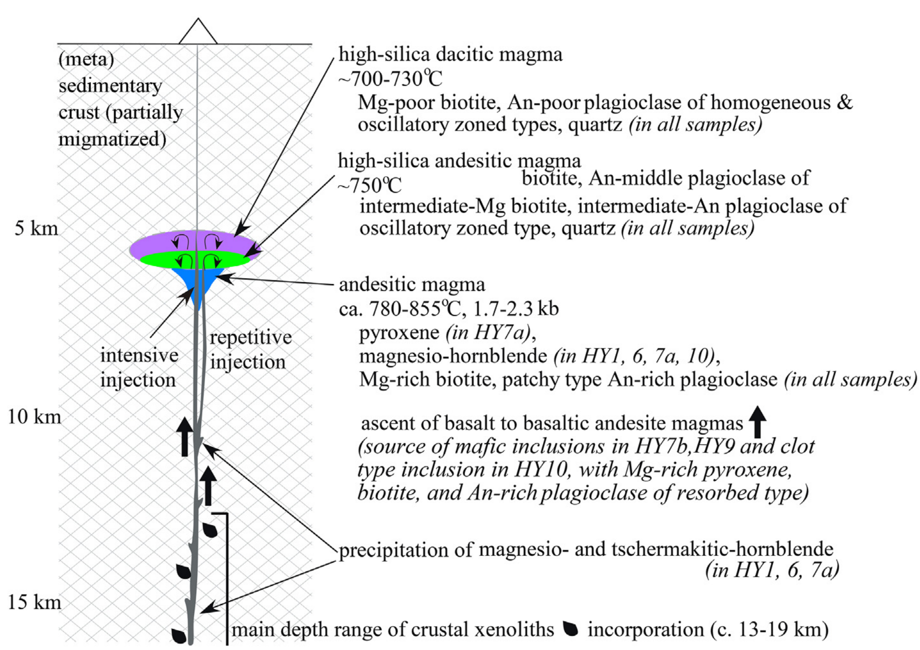

Fig. 15. Sketch summary of the magma plumbing system envisioned beneath El Hoyazo volcano. Regarding the described resorbed and patchy Pl types formed from the deeper ascending magma in the andesitic chamber, both An-poorer rims may have formed during the mixing before eruption. See text for the details.

beneath the main stratified magma chamber. Mg# of hornblendes (ca. 64) and pyroxenes (ca. 70–75) support equilibrium conditions during crystallization. The fairly constant 2.0–2.3 kbar results for the euhedral type and two cases of the opacite rim type suggest a magma reservoir at ~6–7.5 km depth, whereas the higher *P* values may indicate influx of magma batches from ~15 km depth. The subhedral cores and the rest of opacite rim types indicate a wide range of P (ca. 3 kbar difference) revealing polybaric crystallization during ascent whose peak P (~5.0 kbar) is consistent with the range of the entrapping depths of crustal xenoliths (e.g., Álvarez-Valero and Waters, 2010).

4.5. Regional context

As described, El Hoyazo dacites proceeded by mixing between two magma end-members, namely high-SiO_2 andesitic and rhyolitic (or high-SiO_2 dacitic) magmas. This is in line with previous conclusions from crustal xenolith studies in this volcano where magmas from mafic underplating in the Betic Cordillera promoted migmatization (Álvarez-Valero and Waters, 2010) during the first crustal melting event in the NVP. The extracted rhyolitic melt mixed with the mafic (basalts and basaltic andesites) material (Álvarez-Valero and Kriegsman, 2007; Duggen et al., 2004), forming the high-SiO_2 andesites, which in turn mixed with rhyolites extracted from subsequent crustal melting episodes in El Hoyazo (Álvarez-Valero and Waters, 2010).

Only a rapid ascent and magma interaction process (see also Álvarez-Valero et al., 2015; Álvarez-Valero and Waters, 2010) between the deeper magmas transporting crustal restites upward and connecting to higher-SiO_2 melts at shallower depths may explain both the incomplete homogenization of orthopyroxene and clinopyroxene phenocrysts within the bottom andesitic chamber of the shallow stratified magma reservoir and the presence of inherited crustal xenoliths and opacite rim type hornblendes due to deeper magma injections.

5. Conclusions

The present results reveal the existence of a stratified magma reservoir beneath El Hoyazo volcano at ca. 1.7–2.3 kbar (i.e., ~6–7.5 km depth) composed of three layers, from top to bottom: upper level high-SiO_2 dacite (with Mg-poor biotite, An-poor plagioclase and quartz); intermediate level high-SiO_2 andesite (with intermediate-Mg biotite, intermediate-An plagioclase, pyroxene and quartz); and lower level andesite (with euhedral and sieved types of Mg-hornblende, An-rich patchy type plagioclase, and Mg-rich biotite) (Fig. 15). Temperature estimates are ca. 700–730 °C for the upper, ~750 °C for the intermediate, and ~855 °C for the lower parts.

The andesitic magma differentiated to some extent at ca. 780 °C, and was re-injected by hotter (~855 °C) mafic magma. In the latter, pyroxenes (Mg# ~77), and euhedral and sieved types Mg-hornblendes precipitated, and likely also Mg-rich biotites and An-rich plagioclase.

The presence of mafic and clot type inclusions and higher-P hornblendes indicate that the basaltic andesite magmas derived in deeper parts of the magmatic system. Higher P hornblendes were derived from deeper magmas (~5.0 kbar) at ~971 °C, and crystallized at different depths during ascent. Once the magma reached the shallower, stratified chamber, it contributed to increase the internal pressure at the time that it started to mix with the resident magma. In addition, the existence of ortho- and clinopyroxene Mg# values of ~81 and ~ 88, respectively, may indicate the ascent of a significantly undifferentiated basaltic magma.

Resorption textures in phenocrysts are normally related to magma mixing (e.g., Armienti et al., 2007; Firth et al., 2016; Murphy et al., 2000; Nishi et al., 2019) as well as rapid ascent (e.g., Nelson and Montana, 1992). The preservation of sieved textures in the clinopyroxenes and hornblendes, suggests that mixing occurred shortly before the eruption. This is consistent with previous results in El Hoyazo (e.g., Álvarez-Valero et al., 2015, 2016).

Declaration of Competing Interest

The authors declare that they have no known competing financial interests or personal relationships that could have appeared to influence the work reported in this paper.

Acknowledgements

This research was supported by Grant-in-Aid for Scientific Research from the Japan Society for the Promotion of Science (JSPS) to M. Ban (22540487; 17K05701), and USAL-2019 project (Programa Propio - mod. 1B) to A-V. H.H. acknowledges the funded stays at the University of Salamanca (Dept. of Geology and Laboratorio de Isótopos Estables – NUCLEUS) in 2018 and 2019 by the same JSPS grants. We highly appreciate the constructive and in-depth reviews by Joan Martí, Helena Albert and editor Greg Shellnutt that helped to enhance this contribution. We are also grateful to Prof. Emeritus K. Nakajima for assistance in the preparation and observation of thin sections, Takashi Yuguchi and Kae Tsunematsu for valuable suggestions in this study.

References

Albert, H., Costa, F., Martí, J., 2015. Timing of magmatic processes and unrest associated with mafic historical monogenetic eruptions in Tenerife Island. J. Petrol. 56, 1945–1966.
Albert, H., Costa, F., Martí, J., 2016. Years to weeks of seismic unrest and magmatic intrusions precede monogenetic eruptions. Geology 44, 211–214.
Álvarez-Valero, A.M., Kriegsman, L.M., 2007. Crustal thinning and mafic underplating beneath the Neogene Volcanic Province (Betic Cordillera, SE Spain): evidence from crustal xenoliths. Terra Nova 19, 266–271.
Álvarez-Valero, A.M., Kriegsman, L.M., 2010. Chemical, petrological and mass balance constraints on the textural evolution of pelitic enclaves. Lithos 116, 300–309.
Álvarez-Valero, A.M., Waters, D.J., 2010. Partially melted xenoliths as insight into subvolcanic processes: evidence from the Neogene magmatic event of the Betic Cordillera, SE Spain. J. Petrol. 51, 973–991.
Álvarez-Valero, A.M., Cesare, B., Kriegsman, L.M., 2005. Formation of elliptical garnets in a metapelitic enclave by melt-assisted dissolution and reprecipitation. J. Metamorph. Geol. 23, 65–74.
Álvarez-Valero, A.M., Cesare, B., Kriegsman, L.M., 2007. Formation of melt-bearing spinel–cordierite–feldspars coronas after garnet in metapelitic xenoliths. Reaction modelling and geodynamic implications. J. Metamorph. Geol. 25, 305–320.
Álvarez-Valero, A.M., Pla, F., Kriegsman, L.M., Geyer, A., Herrero, H., 2015. Observing silicic magma transport in dikes at depths of 8–19 km: evidences from crustal xenoliths and numerical modelling. J. Volcanol. Geotherm. Res. 296, 69–79.
Álvarez-Valero, A.M., Okumura, S., Arzilli, F., Borrajo, J., Recio, C.M., Ban, M., Gonzalo, J.C., Benítez, J.M., Douglas, M., Sasaki, O., Franco, P., Gómez-Barreiro, J., Carnicero, A., 2016. Tracking bubble evolution inside a silicic dike. Lithos 262, 668–676.
Armienti, P., Francalanci, L., Landi, P., 2007. Textural effects of steady-state behaviour of the Stromboli feeding system. J. Volcanol. Geotherm. Res. 160, 86–98.
Bacon, C.R., 1986. Magmatic inclusions in silicic and intermediate volcanic rocks. J. Geophys. Res. 91, 6091–6112.
Benito, R., López-Ruiz, J., Cebriá, J.M., Hertogen, J., Doblas, M., Oyarzun, R., Demaiffe, D., 1999. Sr and O isotope constraints on source and crustal contamination in the high-K calc-alkaline and shoshonitic Neogene volcanic rocks of SE Spain. Lithos 46, 773–802.
Bigeleisen, J., Perlman, M.L., Prosser, H.C., 1952. Conversion of hydrogenic materials to hydrogen for isotopic analysis. Anal. Chem. 24, 1536–1537.
Bindeman, I., 2008. Oxygen isotopes in mantle and crustal magmas as revealed by single crystal analysis. Rev. Mineral. Geochem. 69, 445–478.
Blake, S., 1981. Volcanism and the dynamics of open magma chambers. Nature 289, 783–785.
Borthwick, J., Harmon, R.S., 1982. A note regarding ClFJ as an alternative to BrF5 for oxygen isotope analysis. Geochim. Cosmochim. Acta 46, 1665–1667.
Cesare, B., Salvioli Mariani, E., Venturelli, G., 1997. Crustal anatexis and melt extraction during deformation in the restitic enclaves at El Joyazo (SE Spain). Min. Mag. 67, 15–27.
Cesare, B., Gómez-Pugnaire, M.T., Rubatto, D., 2003. Residence time of S-type anatectic magmas beneath the Neogene Volcanic Province of SE Spain: a zircon and monazite SHRIMP study. Contrib. Mineral. Petrol. 146, 28–43.
Clayton, R.N., Mayeda, K.N., 1963. The use of bromine pentafluoride in the extraction of oxygen from oxides and silicates for isotopic analysis. Geochim. Cosmochim. Acta 27, 43–52.
Davis, J.C., 2002. Statistics and Data Analysis in Geology. 3rd ed. John Wiley and Sons, New York, p. 638 (ISBN 0-471-17275-8).
Di Battistini, G., Toscani, L., Iaccarino, S., Villa, I.M., 1987. K/Ar age and the geological setting of calc-alkaline volcanic rocks from Sierra de Gata, SE Spain. Neues Jahrb. Mineral. Monatshefte 8, 369–383.
Duggen, S., Hoernle, K., van den Bogaard, P., Harris, C., 2004. Magmatic evolution of the Alboran region: the role of subduction in forming the western Mediterranean and causing the Messinian salinity crisis. Earth Planet. Sci. Lett. 218, 91–108.

Fernández-Soler, J.M., 1996. El volcanismo calcoalcalino en el Parque Natural de Cabo de Gata-Níjar. Estudio volcanológico y petrológico. Monogr. Soc. Almeriense Historia Nat. 2, 295.
Fernández-Soler, J.M., 2001. Volcanics of the Almeria Province. In: Mather, A., Martín, J.M., Harvey, A., Braga, J. (Eds.), A field guide to the Neogene Sedimentary Basins of the Almeria Province, South-East Spain. 350. IAS Field Guide, Blackwell Science, Oxford, UK, pp. 58–88.
Firth, C., Handley, H., Turner, S., Croning, S., Smaith, I., 2016. Variable conditions of magma storage and differentiation with links to eruption style at Ambrym Volcano, Vanuatu. J. Petrol. 57, 1049–1072.
Folch, A., Martí, J., 1998. The generation of overpressure in felsic magma chambers by replenishment. Earth Planet. Sci. Lett. 163, 301–314.
Fonarev, V.I., Konilov, A.N., 1986. Experimental study of Fe-Mg distribution between biotite and orthopyroxene at P=490 MPa. Contrib. Mineral. Petrol. 93, 227–235.
García-Dueñas, V., Balanyá, J.C., Martínez-Martínez, J.M., 1992. Miocene extensional detachments in the outcropping basement of the Northern Alborán Basin (Betics) and their tectonic implications. Geo-Mar. Lett. 12, 88–95.
Gill, J.B., 1981. Orogenic Andesites and Plate Tectonics. Springer-Verlag, p. 392.
Gill, R., 2010. Igneous Rocks and Processes. A Practical Guide. Wiley-Blackwell, p. 428.
Godfrey, J.D., 1962. The deuterium content of hydrous minerals from the east-Central Sierra Nevada and Yosemite National Park. Geochim. Cosmochim. Acta 26, 1215–1245.
Henry, D.J., Guidotti, C.V., Thomson, J.A., 2005. The Ti-saturation surface for low-to-medium pressure metapelitic biotites: implications for geothermometry and Ti-substitution mechanisms. Am. Mineral. 90, 316–328.
Humphreys, M.C.S., Blundy, J.D., Sparks, R.S.J., 2006. Magma evolution and open-system processes at Shiveluch Volcano: insights from phenocryst zoning. J. Petrol. 47, 2303–2334.
Jenkin, G.R.T., 1988. Stable Isotope Studies in Caledonides of SW Connemara, Ireland. PhD Thesis. University of Glasgow, UK.
Johnson, E.R., Wallace, P.J., Cashman, K.V., Granados, H.D., Kent, A.J.R., 2008. Magmatic volatile contents and degassing-induced crystallization at Volcán Jorullo, Mexico: Implications for melt evolution and the plumbing systems of monogenetic volcanoes. Earth Planet. Sci. Lett. 269, 478–487.
Leake, B.E., 1968. A catalog of analysed calciferous and sub-calciferous amphiboles together with their nomenclature and associated minerals. Geol. Soc. Am. Spec. Pap. 98, 210.
Martín, J.M., Braga, J.C., Betzler, C., Brachert, T.C., 1996. Sedimentary model and high-frequency cyclicity in a Mediterranean, shallow-shelf, temperate-carbonate environment (uppermost Miocene, Agua Amarga Basin, Southern Spain). Sedimentology 43, 263–277.
McDonough, W.F., Sun, S.S., Ringwood, A.E., Jagoutz, E., Hofmann, A.W., 1992. Potassium, rubidium and cesium in the Earth and Moon and the evolution of the mantle of the Earth. Geochim. Cosmochim. Acta 56, 1001–1012.
Miyashiro, A., 1974. Volcanic rock series in island arcs and active continental margins. Am. J. Sci. 274, 321–355.
Molina, L., Pulido, A., Sánchez-Martos, F., Vallejos, A., 2015. El Hoyazo de Níjar "Arrecifes y Volcanes" - Guía Geológica de Campo -. Sociedad Geológica de España. https://doi.org/10.13140/RG.2.1.1539.1206.
Murphy, M.D., Sparks, R.S.J., Barclay, J., Carroll, M.R., Brewer, T.S., 2000. Remobilization of andesite magma by intrusion of mafic magma at the Soufrière Hills volcano, Montserrat, West Indies. J. Petrol. 41, 21–42.
Nakamura, M., 1995. Continuous mixing of crystal mush and replenished magma in the ongoing Unzen eruption. Geology 23, 807–810.
Nelson, S.T., Montana, A., 1992. Sieve-textured plagioclase in volcanic rocks produced by rapid decompression. Am. Mineral. 77, 1242–1249.
Nishi, Y., Ban, M., Takebe, Y., Álvarez-Valero, A.M., Oikawa, T., Yamasaki, S., 2019. Shallow magma chamber structure and eruption time scale of the active Zao volcano, NE Japan. J. Volcanol. Geotherm. Res. 371, 137–161.
O'Neill, J.R., 1986. Theoretical and experimental aspects of isotopic fractionation. In: Valley, J.W., Taylor Jr., H.P., O'Neil, J.R. (Eds.), Stable Isotopes in High Temperature Geological Processes, MSA. 16, pp. 1–40.
Pallister, J.S., Hoblitt, R.P., Reyes, A.G., 1992. A basalt trigger for the 1991 eruptions of Pinatubo volcano? Nature 356, 426–428.
Pearce, J.A., Harris, N.B.W., Tindle, A.G., 1984. Trace element discrimination diagrams for the tectonic interpretation of granitic rocks. J. Petrol. 25, 956–983.
Pla, F., Álvarez-Valero, A.M., 2015. Biot number constraints on the sub-volcanic crust-magma thermal regime: an integrating approach of numerical modelling and petrology. In: Caricchi, L., Blundy, J.D. (Eds.), Chemical, Physical and Temporal Evolution of Magmatic Systems. 422. Geological Society, London, Special Publications, pp. 207–216.
Putirka, K.D., 2008. Thermometers and barometers for volcanic systems. Rev. Mineral. Geochem. 69, 61–120.
Reubi, O., Blundy, J., 2009. A dearth of intermediate melts at subduction zone volcanoes and the petrogenesis of arc andesites. Nature 461, 1269–1273.
Ridolfi, F., Renzulli, A., 2012. Calcic amphiboles in calc-alkaline and alkaline magmas: thermobarometric and chemometric empirical equations valid up to 1,130°C and 2.2 GPa. Contrib. Mineral. Petrol. 163, 877–895.
Saunders, A.D., Tarney, J., 1984. Geochemical characteristics of basaltic volcanism within back-arc basins. Geol. Soc. Lond. Spec. Publ. 16, 59–76.
Sengupta, P., Dasgupta, S., Bhattacharya, P.K., Mukherjee, M., 1990. An orthopyroxene–biotite geothermometer and its application in crustal granulites and mantle-derived rocks. J. Metamorph. Geol. 8, 191–197.
Shand, S.J., 1943. Eruptive Rocks: Their Genesis, Composition, Classification, and their Relation to Ore Deposits with a Chaper on Meteorites (Revised). 2nd ed. Hafner Publishing Co., New York.
Sharp, Z.D., 1990. A laser-based microanalytical method for the in situ determination of oxygen isotope ratios of silicates and oxides. Geochim. Cosmochim. Acta 54, 1353–1357.
Soriano, C., Cas, R.A.F., Riggs, N.R., Giordano, G., 2016. Submarine volcanism of the Cabo de Gata Magmatic Arc in the Betic-Rif Orogen, SE Spain. In: Karoly Nemeth, K. (Ed.), Processes and Products, Updates in Volcanology - From Volcano Modelling to Volcano Geology. IntechOpen, pp. 325–354.
Sparks, S.R.J., Sigurdsson, H., Wilson, L., 1977. Magma mixing: a mechanism for triggering acid explosive eruptions. Nature 267, 315–318.
Sun, S.S., 1980. Lead isotopic study of young volcanic rocks from mid-ocean ridges, ocean islands and island arcs. Phil. Trans. R. Soc. A A297, 409–445.
Toscani, L., Venturelli, G., Barbieri, M., Capedri, S., Fernández-Soler, J.M., Oddone, M., 1990. Geochemistry and Petrogenesis of Two-Pyroxene Andesites from Sierra de Gata (SE Spain). Mineral. Petrol. 41, 199–213.
Taylor Jr., H.P., 1967. Oxygen isotope studies of hydrothermal mineral deposits. In: Barnes, H.L. (Ed.), Geochemistry of hydrothermal ore deposits. Holt, Rinehart and Winston 670pp.
Turner, S.P., Platt, J.P., George, R.M.M., Kelley, S.P., Pearson, D.G., Nowell, G.M., 1999. Magmatism associated with orogenic collapse of the Betic-Alborán Domain, SE Spain. J. Petrol. 40, 1011–1036.
Vergés, J., Fernàndez, M., 2012. Tethys-Atlantic interaction along the Iberia-Africa plate boundary: the Betic-Rif orogenic system. Tectonophysics 579, 144–172.
Vissers, R.L.M., Meijer, P.T., 2012. Mesozoic rotation of Iberia: subduction in the Pyrenees? Earth Sci. Rev. 110, 93–110.
Vissers, R.L.M., Platt, J.P., Van Der Wal, D., 1995. Late orogenic extension of the Betic Cordillera and the Alborán Domain: a lithospheric view. Tectonics 14, 786–803.
Weaver, B.L., Tarney, J., 1984. Empirical approach to estimating the composition of the continental crust. Nature 319, 575–577.
Williamson, B.J., Di Muro, A., Horwell, C.J., Spieler, O., Llewellin, E.W., 2010. Injection of vesicular magma into an andesitic dome at the effusive–explosive transition. Earth Planet. Sci. Lett. 295, 83–90.
Yamada, Y., Kohno, H., Murata, M., 1995. A low dilution fusion method for major and trace element analysis of geological samples. Adv. X-Ray Analysis 26, 33–44.
Zeck, H.P., 1970. An erupted migmatite from Cerro de Hoyazo, SE Spain. Contrib. Mineral. Petrol. 26, 225–246.
Zeck, H.P., Kristensen, A.B., Williams, S., 1998. Post-collisional volcanism in a sinking slab setting—crustal anatectic origin of pyroxene-andesite magma, Caldear Volcanic Group, Neogene Alborán volcanic province, southeastern Spain. Lithos 49, 499–522.